Targeting cancer chemotherapy resistance by precision medicine-driven nanoparticle-formulated cisplatin

Siemer, S.; Bauer, T.A.; Scholz, P.; Breder, C.; Fenaroli, F.; Harms, G.; ... ; Stauber, R.H.

Targeting Cancer Chemotherapy Resistance by Precision Medicine-Driven Nanoparticle-Formulated Cisplatin

Svenja Siemer, Tobias A. Bauer, Paul Scholz, Christina Breder, Federico Fenaroli, Gregory Harms, Dimo Dietrich, Jörn Dietrich, Christine Rosenauer, Matthias Barz, Sven Becker, Sebastian Strieth, Christoph Reinhardt, Torsten Fauth, Jan Hagemann, and Roland H. Stauber*

ACCESS | Metrics & More | Article Recommendations | Supporting Information

ABSTRACT: Therapy resistance is the major cause of cancer death. As patients respond heterogeneously, precision/personalized medicine needs to be considered, including the application of nanoparticles (NPs). The success of therapeutic NPs requires to first identify clinically relevant resistance mechanisms and to define key players, followed by a rational design of biocompatible NPs capable to target resistance. Consequently, we employed a tiered experimental pipeline from *in silico* to analytical and *in vitro* to overcome cisplatin resistance. First, we generated cisplatin-resistant cancer cells and used next-generation sequencing together with CRISPR/Cas9 knockout technology to identify the ion channel LRRC8A as a critical component for cisplatin resistance. LRRC8A's cisplatin-specificity was verified by testing free as well as nanoformulated paclitaxel or doxorubicin. The clinical relevance of LRRC8A was demonstrated by its differential expression in a cohort of 500 head and neck cancer patients, correlating with patient survival under cisplatin therapy. To overcome LRRC8A-mediated cisplatin resistance, we constructed cisplatin-loaded, polysarcosine-based core cross-linked polymeric NPs (NP$_{Cis}$, Ø ∼ 28 nm) with good colloidal stability, biocompatibility (low immunogenicity, low toxicity, prolonged *in vivo* circulation, no complement activation, no plasma protein aggregation), and low corona formation properties. 2D/3D-spheroid cell models were employed to demonstrate that, in contrast to standard of care cisplatin, NP$_{Cis}$ significantly ($p < 0.001$) eradicated all cisplatin-resistant cells by circumventing the LRRC8A-transport pathway *via* the endocytic delivery route. We here identified LRRC8A as critical for cisplatin resistance and suggest LRRC8A-guided patient stratification for ongoing or prospective clinical studies assessing therapy resistance to nanoscale platinum drug nanoformulations versus current standard of care formulations.

KEYWORDS: nanomedicine, cisplatin resistance, rational design, personalized medicine, polypept(o)ides
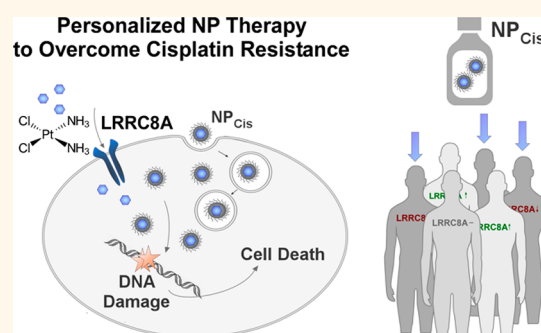
Cancer is one of the main causes for human hospitalizations and deaths globally.[1,2] Classical cancer treatments include surgical removal, radiotherapy, and (immuno-)chemotherapy. Despite the initial treatment success of chemotherapeutics, the development of therapy-resistance over time is the main cause for deaths for all types of cancer, urging for improved strategies to overcome resistances.

The rapid progress in nanotechnology combined with our increased knowledge of the complex cross-talk at nanobio interfaces has raised high expectations in nanomedicine to also combat cancer, including therapy resistances.[3−5] Numerous delivery and theranostic nanotools have been developed to date, often claiming to be superior to small molecule chemotherapeutics due to sustained drug release, better cancer

cell uptake, enhanced permeation and retention (EPR) effect in tumors, prolonged bioavailability, and less side-effects.[6−10] Impressive developments also include the design of multifunctional nanotools, allowing codeliveries of drugs with siRNAs or peptides as well as the addition of active tumor cell targeting decoys, such as antibodies, aptamers, or peptides onto the NPs' surfaces.[11−15] Moreover, NPs have been reported to better kill
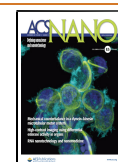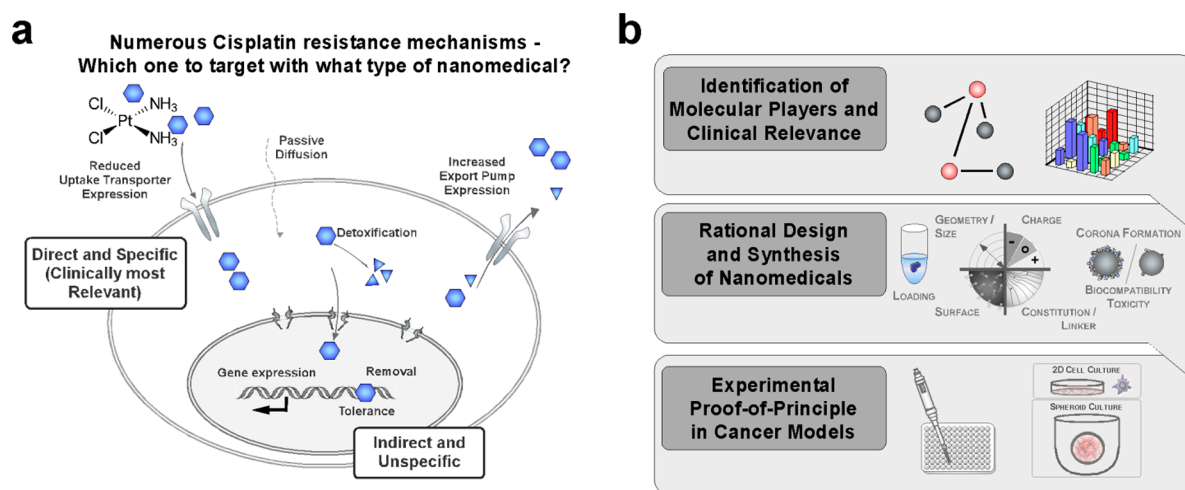
Figure 1. Summary of suggested cisplatin resistance mechanisms and experimental pipeline to overcome chemoresistance. (a) Illustration summarizing suggested main cellular cisplatin resistance mechanisms. Reducing the drug's intracellular concentration may result from a reduced expression of drug uptake transporters, increased expression of drug efflux pumps, enhanced drug detoxification, improved DNA repair as well as additional prosurvival signaling pathways. Cisplatin and cell compartments are indicated. Not drawn to scale. (b) Illustration summarizing the study's tiered experimental targeting strategy.

resistant cancer cells through enhanced cell internalization, stimuli-responsive drug release, inhibition of drug efflux, and more. However, postulated effects have not always been investigated sufficiently or understood mechanistically and multifunctional nanotools have not reached the clinic yet.[16]

Nevertheless, the use of nanoscale platinum drug delivery devices (soft or hard nanoparticles, such as Lipoplatin, SPI-077 or NC-6004) as potential alternatives have entered (pre)-clinical studies.[6,17−19] Among these, the small-sized polymeric micelles of NC-6004 currently exhibit the greatest potential for clinical translation (phase III). The evolution of NC-6004 from poly(asparagine) to poly(L-glutamic acid) as the functional polymer block provided a stable yet reversible conjugation of cisplatin.[6,20−22] Despite these advances, the successful clinical translation of such nanomedicals, particularly of 'hard' NPs, is still limited. Notably, besides safety/toxicity considerations for the active drug, it is expected and desired that nano-encapsulation is changing the pharmacokinetics of a drug, which needs to be taken into consideration for the application.[23] Moreover, the biocompatibility of the used nanocarriers, including biomolecule corona formation, needs to be examined as well. It is accepted that, when NPs enter (patho)physiological environments, proteins and other bio-molecules bind to the nanomaterial surface, leading to the rapid formation of a biomolecule corona. The corona may be critically codefining the biological, medical, biotechnological, and pathophysiological identity of NPs, although the mechanistic details have not been resolved in detail.[24−30] As the impact of the corona can still not be predicted reliably, the design of NPs with low biomolecule adsorption properties is desirable and can be achieved by several chemical function-alization strategies.[31,32] Here, the use of polypept(o)ide-based formulations promise good colloidal stability, biocompatibility (low immunogenicity, low toxicity, prolonged *in vivo* circulation, no complement activation, no plasma protein aggregation), and low corona formation properties. Polypept-(o)ides are hybrid copolymers combining polypeptides with the polypeptoid polysarcosine (pSar, poly(*N*-methyl glycine)), which is biologically well-tolerated.[60,61] pSar is considered a promising alternative to poly(ethylene glycol), showing

advantages of reduced proinflammatory cytokine secretion, reduced complement activation, and evasion of the accelerated blood clearance (ABC) phenomenon.[62−65]

However, despite the impressive progress on potential nanomedicals, their clinical applicability and superiority compared to drug formulations used in the clinical routine for decades needs to be based on a mechanistic understanding of their advantages.[3,5,33]

First-line chemotherapy of head and neck cancers (HNSCC) is predominantly platinum-based with cisplatin being the primary option despite its drawbacks like severe nausea, dose-limiting nephrotoxicity, myelosuppressive effects, ototoxicity, or peripheral neuropathy.[34−36] Differences in the toxic effects of platinum compounds are mainly due to their chemical reactivity, but they seem also to be influenced by the expression of organ/cell-specific drug transporter/detoxifica-tion machineries.[6,37−42]

Resistance to chemotherapeutics, such as platinum-based drugs, on the individual, organismal as well as on the cancer cell level are manifold, complex, and not yet fully under-stood.[6,37−39] Especially in HNSCC as well as in other malignancies, therapy-resistant relapses are common due to molecularly highly heterogeneous cell populations[34] and associated with high patient morbidity.[43,44] Main clinically relevant effects impact the drug's intracellular concentration and induced DNA damage, ultimately triggering cancer cell death (Figure 1a).[40−42] Cisplatin-resistant cancer cells may show a wide range of responses, including decreased cellular drug uptake, increased drug efflux, enhanced DNA repair, improved drug detoxification as well as additional prosurvival signaling pathways.[42] Adding even another level of complexity, it is accepted that, depending on the type of resistance mechanism combined with their (epi)genetic fingerprints, patients may respond differently to (nano)therapeutics, necessitating precision/personalized treatments.[18,45] The field, including the FDA, thus started to move away from block-buster treatments for all patients who may not profit but rather suffer from often expensive therapeutics. Examples for such precision/personalized treatments from the current clinical routine are therapeutic antibodies for the treatment
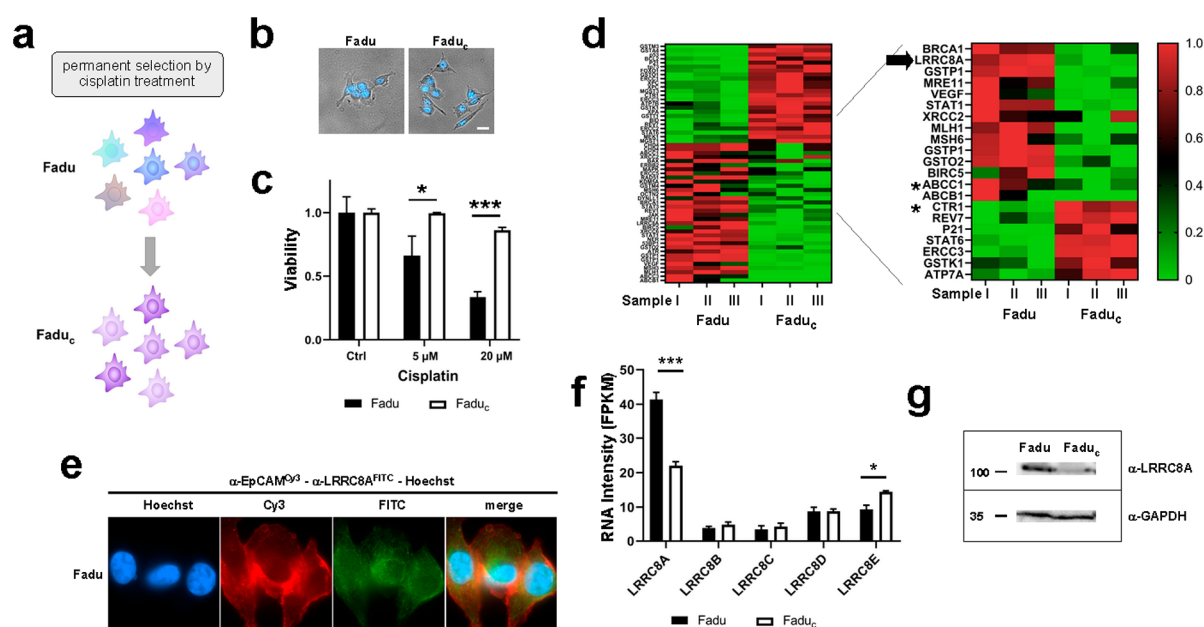
Figure 2. Identification of molecular players most relevant for cisplatin resistance. (a) Illustration of selection process to establish cisplatin-resistant Fadu$_C$ cells. (b) Similar cell morphology visualized by microscopy. Nuclei stained with Hoechst dye (blue). Scale bar, 20 μm. (c) Fadu$_C$ are highly cisplatin-resistant. Cells treated for 48 h and viability normalized to untreated controls. (d) RNASeq-transcriptomics to identify cisplatin resistance candidates. Heatmap analysis of FPKM values visualizing genes differentially expressed in cisplatin sensitive (Fadu) versus resistant (Fadu$_C$) cells (green, downregulated; red, upregulated; full list of genes and raw expression data in Tables S5 and S6). Potentially most relevant transporter genes LRRC8A, CTR1, and ABCC1 are marked. (e) Immunofluorescence detection of EpCAM and LRRC8A. Cells were stained with indicated antibodies. Scale bar, 5 μm. (f) Differential expression of LRRC8 components. LRRC8A expression was significantly reduced in cisplatin-resistant (Fadu$_C$) cells; LRRC8E slightly upregulated. RNA intensities (FPKM) in $n = 3$ samples shown. Statistical analysis by unpaired Student's t test. *, $p < 0.05$; ***, $p < 0.005$. (g) Immunoblot analysis confirming decreased protein levels of LRRC8A in Fadu$_C$ cells. GAPDH served as a loading control. Cells were stained with indicated antibodies. MW (kD) is indicated.

of EGFR-expressing head and neck and colorectal tumors or Her2-positive breast cancers, as well as the application of kinase inhibitors/therapeutic antibodies for *Ras*-mutated lung cancers.[46−49]

The aim of the study was to develop a nanomedical-based strategy to overcome therapy resistance as part of a potential personalized medicine approach. Designing successful therapeutic NPs to break chemoresistances requires to first identify clinically relevant (personalized) cancer resistance mechanisms and key players followed by a rational design and application of targeted NPs to overcome the identified resistances (for overview and experimental strategy see Figure 1 and Figure S1).

Consequently, we here employed a tiered experimental pipeline from *in silico* to analytical and *in vitro* to overcome cisplatin resistance in head and neck cancer as a clinically relevant model. Collectively, we identified the ion channel LRRC8A as a critical component for cisplatin-specific uptake and resistance, confirmed its potential clinical relevance, and applied cisplatin-loaded NPs to kill cisplatin-resistant cells by bypassing the LRRC8A-transport pathway. The strategy and results of our study may aid the personalized application of nanomedicals to overcome chemotherapy resistance in general.

RESULTS/DISCUSSION

Identification of Molecular Pathways and Key Players of Cisplatin Resistance. Focusing on HNSCC as a clinically highly relevant disease entity, we first generated cell culture models to identify molecular cisplatin resistance mechanisms, which is not trivial for an effective anticancer drug. While

tumors in patients contain >10^9 cells as a starting population to select cisplatin-resistant (stem)cell clones over months or years, *in vitro* cell cultures start with much lower cell numbers and a less heterogeneous phenotypic population. However, a homogeneous cisplatin-resistant cell line favors the identification of resistance pathways by molecular 'omics' methods. By selecting HNSCC Fadu cells with subtoxic concentrations of cisplatin (3−5 μM) for six months, we successfully established a cisplatin-resistant cell line, Fadu$_C$ (Figure 2a). Compared to the parental Fadu$_{WT}$ cells, Fadu$_C$ cells were highly resistant to cisplatin (∼2 versus ≤20 μM). Macroscopically, Fadu$_C$ did not show differences to the initial cell population (Figure 2b). Of note, the cisplatin-resistant phenotype was maintained even when Fadu$_C$ cells were cultured in the absence of cisplatin for up to one month, indicating that stable genetic alterations have occurred. This marked Fadu$_C$ cells an ideal tool to identify HNSCC resistance mechanisms. Thus, we next performed next-generation RNA sequencing to obtain genome-wide transcriptomics profiles. Although current bioinformatic algorithms seem to facilitate the comparison and (meta-)analysis of gene expression data generated by different profiling platforms from databases, it is accepted that optimal results are obtained by using the same platform. To reduce intrinsic technical variations, generating 'data noise' and potentially occluding data reliability, we analyzed the samples in three independent replicates in a single experiment.

The comprehensive data sets were subsequently bioinformatically analyzed to identify genes differentially expressed between cisplatin sensitive and resistant cells (see Figure S1
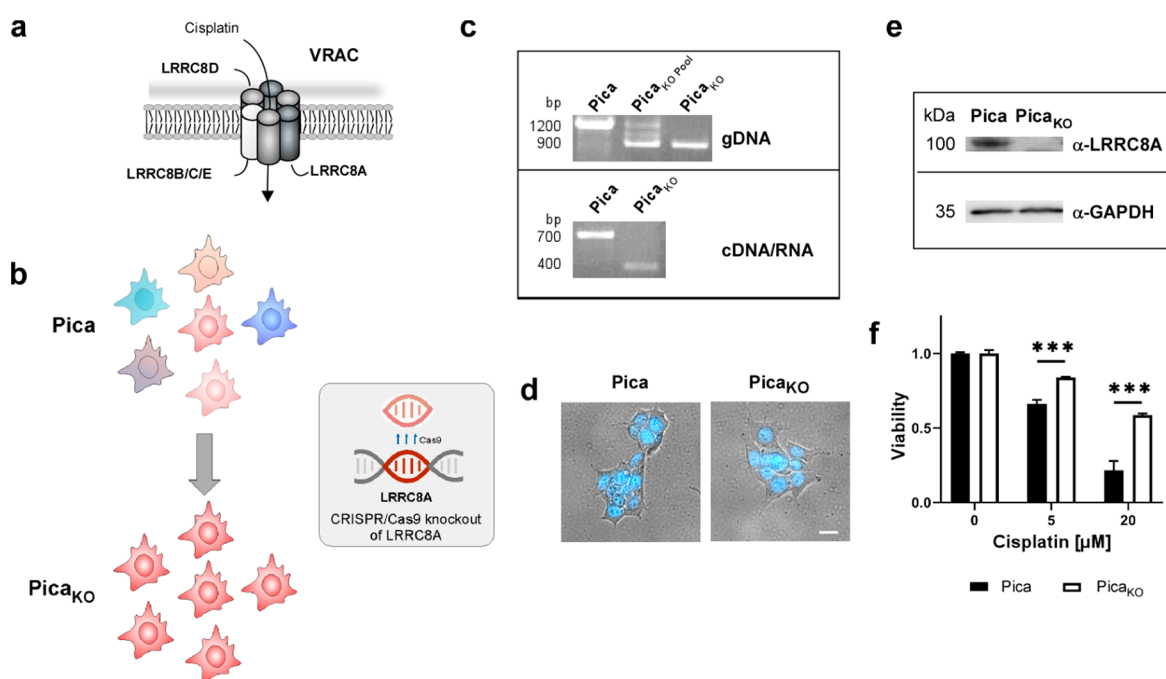
Figure 3. LRRC8A is critical for cisplatin response. (a) Scheme of the VRAC channel, consisting of six heteromeric subunits. LRRC8A is critical for function, subunits LRRC8B/C/D/E suggested to further contribute to substrate specificity. (b) Generation of LRRC8A-deficient knockout cells (Pica$_{KO}$) by CRISPR/Cas9 technology. (c) Knockout was confirmed on the genomic DNA and RNA/cDNA levels. For primer design and location, see Figure S4. (d) Similar cell morphology of Pica and Pica$_{KO}$ visualized by microscopy. Nuclei were stained with Hoechst dye (blue). Scale bar, 20 μm. (e) Immunoblot analysis confirming the absence of LRRC8A protein in Pica$_{KO}$ cells. GAPDH served as the loading control. Blots were stained with indicated antibodies. MW (kD) is indicated. (f) LRRC8A-deficient Pica$_{KO}$ cells are highly cisplatin-resistant. Cells were treated for 48 h, and viability was normalized to untreated controls.

and Table S6). Here, genes significantly differentially expressed ($p < 0.05$ as the cutoff) in our cisplatin-resistant cell model were selected by strictly following established protocols. As the data volume and complexity from RNA-seq experiments necessitate fast, scalable, and mathematically principled analysis, we used the approaches described in detail in the excellent works of Love *et al.* and Trapnell *et al.*, mainly using *TopHat*, *Cufflinks*, and negative binomial distribution assisted by *DESeq2* to perform such analyses.[86,87] Our protocol begins with raw sequencing reads and produces a transcriptome assembly, lists of differentially expressed and regulated genes and transcripts (see Tables S5 and S7 and heatmap in Figure 2d, left). As indicated also in Table S5, it is not uncommon to find genes with relatively small fold changes (*e.g.*, less than 2-fold) in expression marked as significant. This reflects the high overall sensitivity of RNA-seq compared with other whole-transcriptome expression quantification platforms. We identified potential factors involved in cisplatin resistance by transcriptomics relying on significantly differentially transcribed genes in our cell model (Figure 2 and Table S8; summarized in Tables S6 and S7). Table S7 lists the most significant genes that were up- or downregulated with their respective gene IDs and locus, absolute values, and ratios ranked by significance. Notably, the data set showed good correlation of the three independent replicates, confirming the experimental quality and reliability of the data, a prerequisite for their subsequent bioinformatic exploitation.

As several proteins have already been suggested to be directly or indirectly involved in influencing cisplatin resistance,[42,50,51] we additionally performed supervised analyses of such factors, supported by *Ingenuity/Reactome* pathway tools,[52] and further meta-analyses including overall survival

Kaplan–Meier curves of *The Cancer Genome Atlas* collective (Figures S2 and S3). Hierarchical clustering was performed on a selected subset of 58 of these candidates (Figure 2d left; Table S5). The candidates were further condensed on the basis of their highest potential as relevant cisplatin resistance factors (Figure 2d, right) (Figure S1). Besides, indirect contributors such as cell signaling and/or cell cycle regulators (*e.g.*, STATs, p21) or proteins known to be involved in detoxifications processes of metal ions, such as glutathione conjugation enzymes (*e.g.*, GSTK1) and (metal) ion/small molecule uptake and export transporters (*e.g.*, CTR1, ABC/MDR, LRRC8A, MRP1)[16,53−55] were significantly differentially expressed. Notably, in contrast to other studies reporting for example enhanced expression of the (metal) ion/small molecule export transporter MRP1,[16] we found its reduced expression in the cisplatin-resistant cells. Likewise, the drug uptake transporter CTR1 was upregulated in the cisplatin-resistant cells, in contrast to other reports.[54] Of note, none of these studies performed a direct genome-wide comparison of relevant resistance factors employing sensitive vs resistant models.

Drug Uptake Transporter Component LRRC8A is a Critical Determinant for Cisplatin Resistance. As a strong candidate for cisplatin uptake and resistance in our data set, we further investigated LRRC8A, significantly downregulated in all of the cisplatin-resistant cell samples. LRRC8A is the constituting member of the volume-regulated anion channel (VRAC), a heteromer constituted of six subunits, composed of LRRC8A/B/C/D and E (Figure 3a).[56,57] Its differential expression has been suggested to additionally affect various tumor cell survival pathways, including (selective) drug uptake and resistance.[53,56,57] For our HNSCC models, we confirmed LRRC8A's membranous expression and down-regulation in
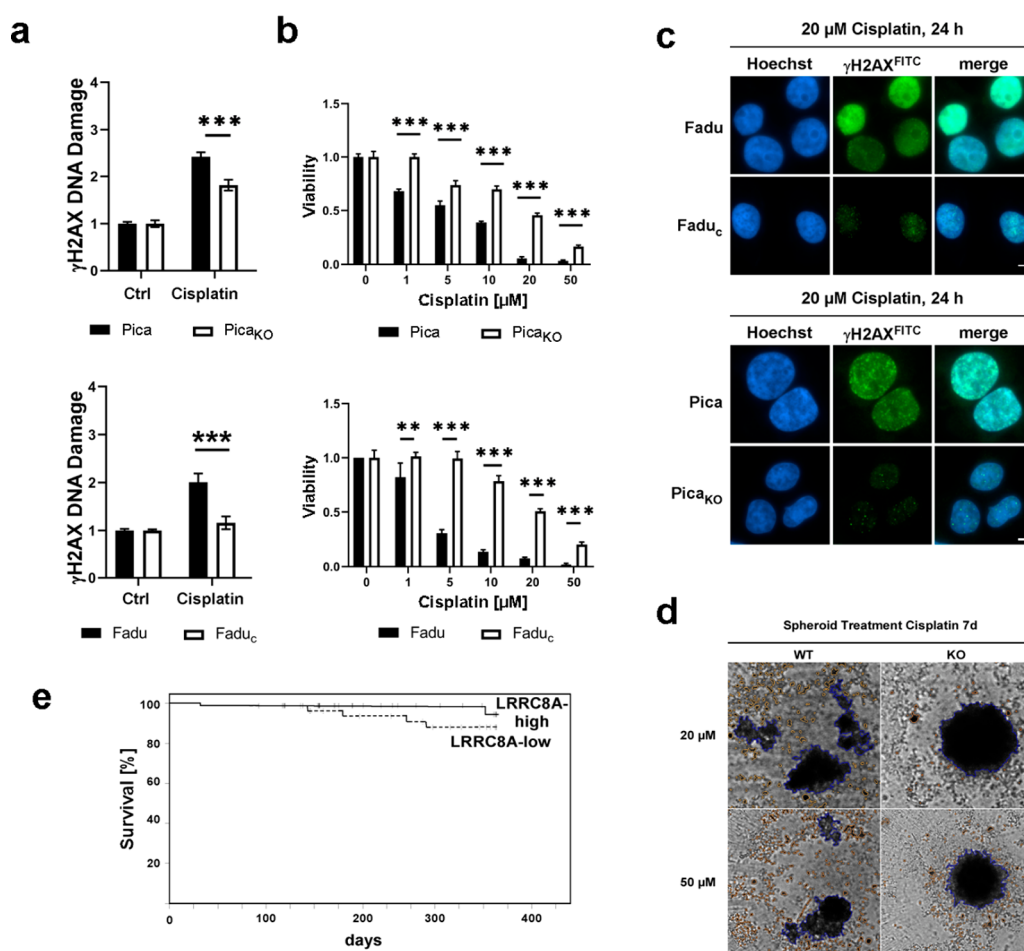
Figure 4. Low LRRC8A levels protect against cisplatin-induced DNA damage and cancer cell death and correlate with patients' chemoresistance and survival. (a−c) Reduced number of cisplatin DNA damage events (γH2AX foci) in resistant, LRRC8A low/deficient, cells. (a) Automatic quantification of γH2AX foci *via* high-throughput automated microscopy. Cells were treated for 24 h, and DNA damage events were normalized to untreated controls. (b) Induction of cancer cell deaths correlates with cisplatin-induced DNA damage. Cells were treated for 48 h, and viability was normalized to untreated controls. (c) Detection of cisplatin-induced DNA damage events (γH2AX foci) by immunofluorescence microscopy, 24 h post-treatment. γH2AX foci were detected by specific antibodies. Scale bars, 5 μm. (d) LRRC8A-mediated resistance is relevant also for 3D tumor-spheroids. In contrast to killed $Pica_{WT}$ spheroids, $Pica_{KO}$ spheroids stay viable even after prolonged treatment with high cisplatin concentrations. Microscopy images after treatment for 7d. (e) Low LRRC8A expression levels, favoring resistance of tumor cells, indicate reduce survival of cisplatin treated HNSCC patients ($n = 78$) shown by Kaplan−Meier plots; $p = 0.26$.

the resistant cell line not only at the RNA but also on the protein level by immunoblot analyses (Figure 2e−g). In contrast to reduced LRRC8A levels, the other subunits were equally expressed, and we found a slight upregulation of LRRC8E (Figure 2f). Although LRRC8A is the constituting subunit and, thus, mainly responsible for cisplatin uptake, also LRRC8D was suggested to further contribute to efficacy and specificity of drug uptake.[56−58] However, the molecular details are not fully understood and we did not detect relevant differences in LRRC8D transcription in our KO or cisplatin-resistant cell lines (Figure S6). Hence, we subsequently focused on LRRC8A.

To unambiguously verify LRRC8A's role in cisplatin resistance, we performed its CRISPR/Cas9 knockout (KO) in the HNSCC cell line Pica as an additional independent cell model. Underlined by the Nobel prize award to the CRISPR/Cas9 technology, this method allows to exclusively eliminate the LRRC8A protein without inducing other genetic alterations (Figure 3). For maximal comparability and genetic homogeneity, different single cell KO clones were generated

and thoroughly characterized (Figure 3c−e, Figure S4, and Table S3). Analytical PCRs on gDNA and cDNA level verified LRRC8A depletion, which was further confirmed by immunoblot analysis in the resulting cell line $Pica_{KO}$ (Figure 3c,e and Figure S5). Importantly, LRRC8A depletion alone was sufficient to confer cisplatin resistance, underlining its relevance as a key cisplatin resistance factor (Figure 3f). Hence, other factors suspected by previous studies do not seem to contribute significantly to resistance of our cancer models, although LRRC8A expression was not examined in these studies.[16,51,54] Also, the reported specific reduction of MRP1 expression by cisplatin-resistance-braking NPs cannot be explained mechanistically and certainly requires further detailed analysis.[16,54]

Again, the cisplatin-resistant cell line $Pica_{KO}$ was morphologically similar to the sensitive parental cell line (Figure 3c). As an additional control, we verified that the identified mechanism is specific for cisplatin. None of the cell lines showed cross-resistance to clinically employed chemotherapeutics, such as paclitaxel or doxorubicin, either when
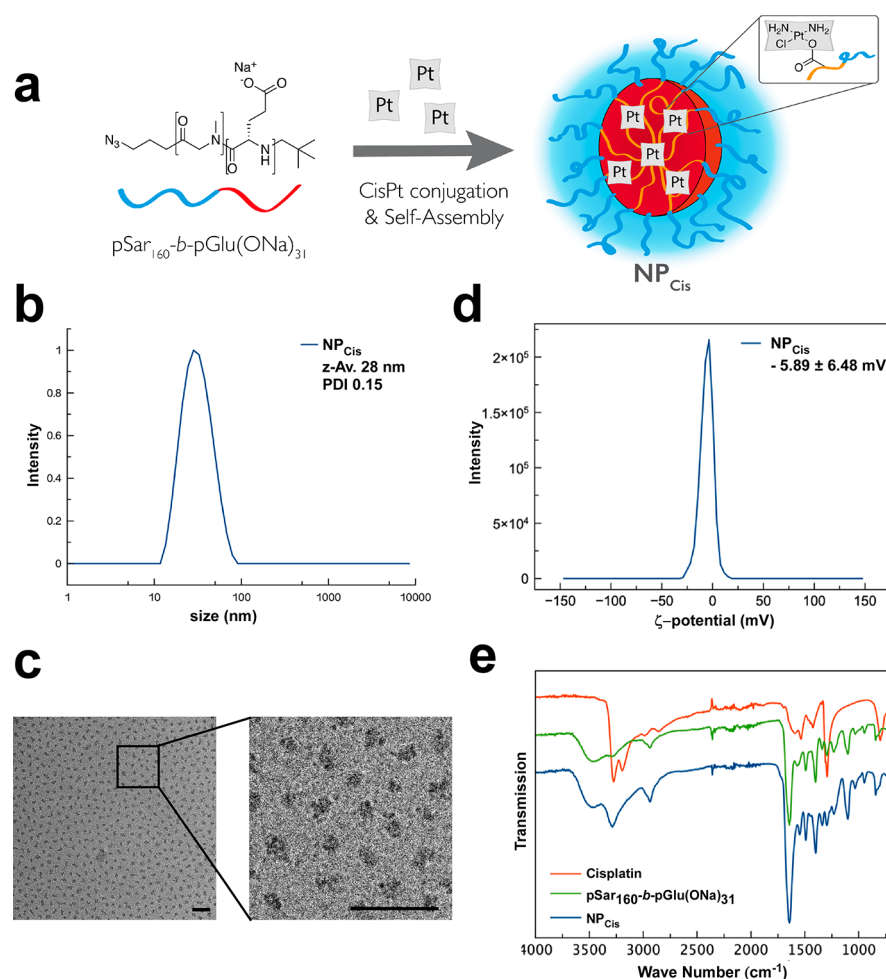
Figure 5. Design and characterization of cisplatin-loaded polymeric micelles (NP$_{Cis}$). (a) Illustration of polysarcosine-*block*-poly(glutamic acid) (pSar$_{160}$-*b*-pGlu(ONa)$_{31}$) building blocks, cisplatin conjugation, and expected NP$_{Cis}$ structure (b) Dynamic light scattering (DLS) analysis shows a z-average size of Ø ~ 28 nm and a narrow PDI of 0.15. (c) Cryo-EM analysis confirms the shape, size, and homogeneity of NP$_{Cis}$. Scale bars, 50 nm. (d) NP$_{Cis}$ shows a neutral ζ-potential. (e) FT-IR spectroscopy confirms the successful coupling of cisplatin and pSar$_{160}$-*b*-pGlu(ONa)$_{31}$.

employed as a free drug or as nanoformulations, *e.g.*, Abraxane/Caelyx (Figures S8 and S9).

Notably, cisplatin resistance through LRRC8A depletion was confirmed not only in 2D conventional cell cultures but also in 3D tumor spheroids, mimicking more closely the tumor microarchitecture in patients without having to rely on LRRC8A knockout animal models, which show multiple physiological impacts and defects.[59] Pica$_{KO}$-derived tumor spheroids remained intact and viable even after prolonged treatment with high concentrations of cisplatin, while LRRC8A expressing wildtype cells were efficiently killed (Figure 4b, d).

The main direct cisplatin toxicity mechanism is the induction of DNA breaks, triggering apoptosis. If cisplatin uptake is reduced by low LRRC8A levels, reduced cisplatin-induced DNA damage should occur in the resistant cell lines. We therefore applied automated high content quantification as well as conventional microscopy to probe γH2AX DNA damage foci (Figure 4a,c and Figure S7). Indeed, reduced DNA damage was detected, confirming our hypothesis (Figure 4a,c and Figure S7).

Collectively, we here established low-LRRC8A HNSCC cisplatin-resistant cell lines by cisplatin selection as well as by CRISPR/Cas9 knockout of LRRC8A, clearly demonstrating its

key relevance for cellular cisplatin transport, cancer cell death and, thus, drug resistance.

Clinical Relevance of LRRC8A Expression Levels in HNSCC Patients. Key for the success of precision/personalized (nano)medicine is the identification of bio-markers to stratify patients who will most likely profit from treatments. For example, assessing Her2 expression in breast cancers prior to immunotherapy increased therapy success from 25% to 70%.[46,47] Thus, to further validate our preclinical findings, we examined the transcriptomics data set of HNSCC patients from The Cancer Genome Atlas (TCGA) (n = 473). Interestingly, LRRC8A expression levels varied widely in tumors in contrast to healthy adjacent tissue (Figure S10a). As LRRC8A is suspected to also support tumor cell survival pathways in addition to drug uptake,[56,57] such heterogeneity can be expected. To investigate cisplatin therapy-specific effects for patient survival, we analyzed the overall survival for patients that received cisplatin (n = 73). The expression data from the TCGA cohort were used to select HNSCC patients with high and low LRCC8A gene expression (Figure S10). As cisplatin therapy acts rather rapidly, we restricted our analysis to one year. On the basis of our data, we hypothesized that low LRCC8A expression, *i.e.*, reduced uptake of cisplatin,
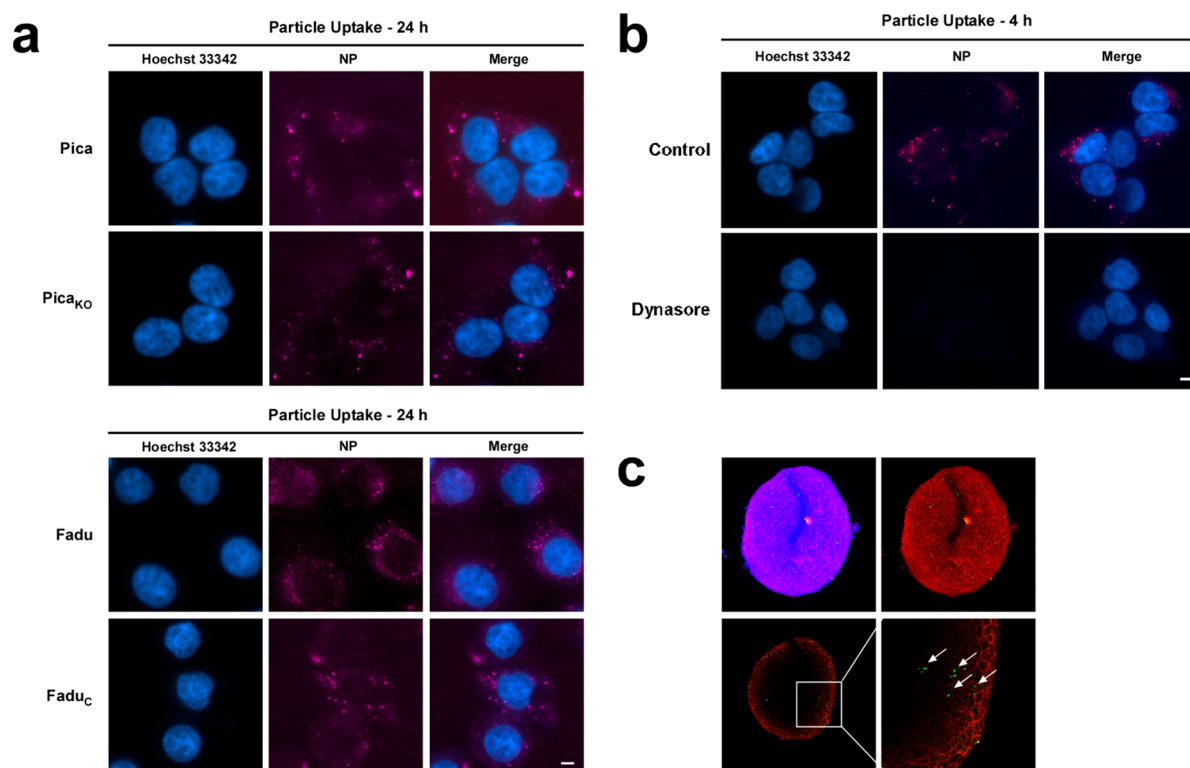
Figure 6. NP uptake does not require the LRRC8A ion channel but is mediated by endocytosis. (a) Uptake of polymeric NPs (Atto647N) occurs in LRRC8A-deficient knockout (Pica$_{KO}$)/low (Fadu$_C$) and LRRC8A high WT cells (Pica)/(Fadu). Cells were treated for 24 h. Nuclei marked in blue. Scale bars, 5 μm. (b) Uptake is prevented by treatment (10 min) with endocytosis inhibitor dynasore (40 μM). Excitation time fixed at 5000 ms for image acquisition. Scale bar, 5 μm. (c) Two-photon microscopy shows NPs penetrating 3D tumor spheroids. Spheroids (3D) were treated with NP^{green} (6 μg/mL, green) for 48 h. Spheroids were stained for cell surface EpCAM expression (red) and nuclei (blue). Lower panel: representative image of single z-plane. White arrows mark intraspheroid NPs.

favors cancer cell survival, which may lead to tumor recurrences ultimately causing patient death. Indeed, a trend in the Kaplan–Meier curve of overall survival indicates that patients with low LRCC8A expression displayed a reduced survival ($p = 0.26$) (Figure 4e). This trend was lost when all patients were analyzed ($p = 0.46$), suggesting that cisplatin treatment might act as selection pressure *in vivo* (Figure S10b). Further comprehensive prospective clinical studies in various malignancies are clearly required to fully validate the prognostic value of LRCC8A expression for cisplatin therapy and the application of potentially therapeutic nanomedicals to overcome resistances in general.

Currently, there is ongoing (pre)clinical research to decide if and what types of nanoscale platinum drug delivery devices are indeed superior compared to the current standard of care formulations for certain tumor types and cancer patients, including HNSCC.[6,17,18] Particularly, it would be important to guide clinical studies of therapeutic nanomedicals, such as NC-6004 (NCT: NCT00910741),[6] by LRCC8A-based patient stratification in order to better reveal their therapeutic benefits.

Rational Design and Synthesis of NP Formulations to Overcome LRRC8A-Mediated Cisplatin Resistance. Having confirmed LRRC8A-mediated resistance as well as its clinical relevance, we investigated chemical strategies to overcome cisplatin resistances. As reconstitution of the cisplatin uptake channel by small molecules or NPs is quite unlikely, we subsequently aimed at increasing intracellular cisplatin concentrations by nanoformulation-mediated endocytic uptake, thereby circumventing LRRC8A-mediated drug resistance. Consequently, cisplatin-loaded, polysarcosine-based

core cross-linked polymeric NPs (NP$_{Cis}$) were designed for cancer-targeted drug delivery. NP$_{Cis}$ were synthesized from polypept(o)ides of polysarcosine-*block*-poly(glutamic acid) (pSar-*b*-pGlu), and cisplatin was conjugated to the pGlu-block *via* ligand exchange (Figure 5a). Polypept(o)ides are hybrid copolymers combining polypeptides with the poly-peptoid polysarcosine (pSar, poly(N-methyl glycine)), which is biologically well-tolerated.[60,61] Polysarcosine is a weak hydrogen bond acceptor and highly soluble in aqueous solution adopting a random coil conformation. As such, pSar is considered a promising alternative to poly(ethylene glycol), showing advantages of reduced proinflammatory cytokine secretion, reduced complement activation, and evasion of the accelerated blood clearance (ABC) phenomenon.[62−65] The biocompatibility and absence of detectable toxicity of pSar-*b*-pGlu was verified for our cell models by exposing cells for 48 h (Figure S11). In combination with pSar, the functionality of polypeptides was further exploited for the design of core−shell architectures. The use of building blocks based on natural amino acids like glutamic acid is a promising strategy to facilitate biodegradability, which is a critical *in vivo* safety factor.[66,67] For pSar-*b*-pGlu(ONa), block copolymers were prepared from γ-tert butyl-L-glutamate NCA, followed by the polymerization of sarcosine NCA. For the preparation of NP$_{Cis}$, block lengths of 160 for pSar and 31 for pGlu were used, accounting for steric shielding and assembly to small spherical structures (Figure 5a,c). The conjugation of cisplatin induced the self-assembly of the hydrophilic pSar$_{160}$-*b*-pGlu(ONa)$_{31}$, yielding polymeric micelles with a diameter of $\varnothing \sim 28$ nm and a narrow PDI of 0.15 (Figure 5b). Our NP size was reported to
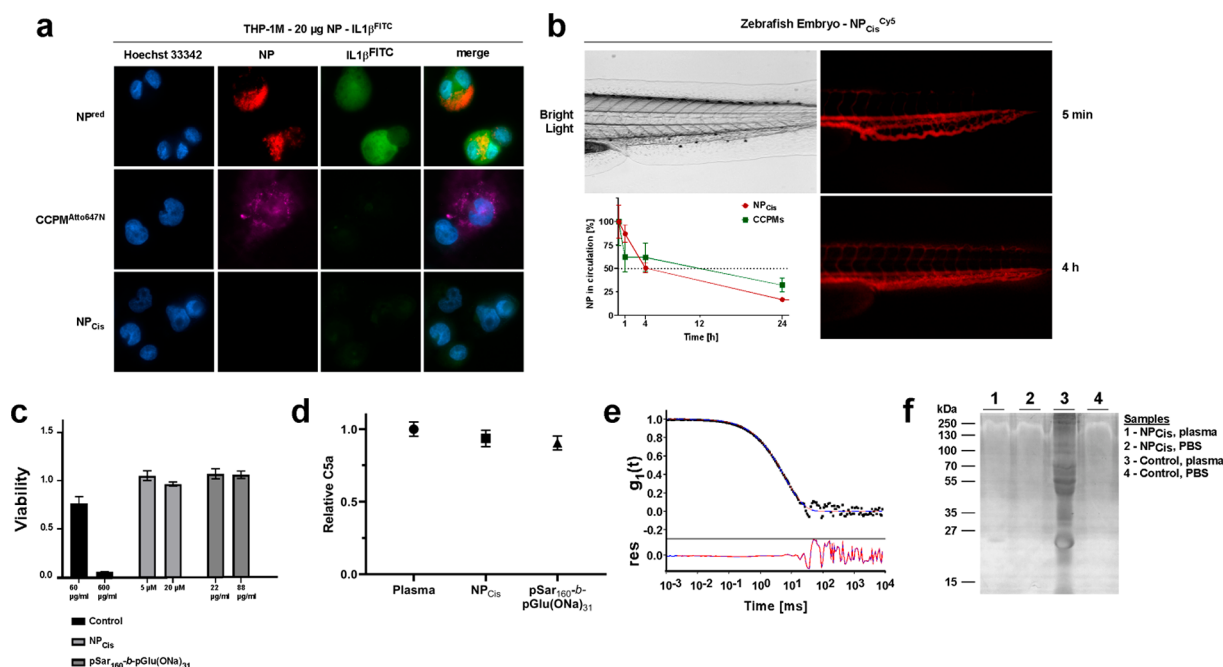
Figure 7. Cisplatin-loaded polymeric micelles (NP_{Cis}) show good *in vitro* and *in vivo* biocompatibility and low corona formation properties. (a) NP_{Cis} do not trigger macrophage activation. Differentiated THP-1 M macrophages do not produce IL-1β when treated with NP_{Cis} (lower panel) or unloaded fluorescent polysarcosine control particles (CCPMs; middle panel). In contrast, exposure to fluorescent silica NPs (NP^{red}) with high corona formation properties strongly induced IL-1β production (upper panel). Cells were treated with indicated NPs (20 μg each) for 24 h before cells were fixed and immunofluorescent stained for IL-1β (green). Cell nuclei, blue. Fluorescently labeled NPs, red. Scale bar, 5 μm. (b) pSar NPs display reduced recognition by the reticuloendothelial system resulting in prolonged blood circulation. Fluorescently labeled NP_{Cis} (NP_{Cis}^{Cy5}) or covalently linked polysarcosine control particles (CCPMs) were injected into zebrafish embryos and circulation analyzed by *in vivo* imaging microscopy for up to 24 h. Bright light image of a zebrafish tail containing circulating fluorescent NPs (upper left panel). Fluorescence microscopy images of a zebrafish tail containing circulating NP_{Cis}^{Cy5} at indicated time points (left, lower panel). Quantification of the circulation half-life for indicated NPs based on the average fluorescence intensity of the artery region normalized by the average total fluorescence of the zebrafish. Circulation half-life: $NP_{Cis}^{Cy5} \approx 4$ h; CCPMs ≈ 12 h (lower left panel). (c) NP_{Cis} or the polysarcosine polymer show no short-term toxicity. Cells were treated for 4 h, and viability was normalized to untreated cells. In contrast, exposure to silica NPs (control) with high corona formation properties rapidly triggered cell death at higher concentrations. (d) NP_{Cis} do not trigger complement activation. Human plasma was untreated or exposed to NP_{Cis} or the respective polysarcosine-*block*-poly(glutamic acid) polymer (37 °C, 1 h) and levels of C5a as an indicator for complement activation quantified by ELISA. (e) NP_{Cis} display good colloidal stability and do not induce human plasma protein aggregation. Multiangle DLS measurements were performed in plasma in the presence of NP_{Cis}. Temperature 37 °C, $t = 1$ h. Upper graph: Autocorrelation function $g_1(t)$ for the exemplary scattering angle of 30° together with fits without (red) and with (blue) additional aggregate term. Lower graph: Calculated residuals between the respective fit and the correlation function. (f) Low corona formation on NP_{Cis} after incubation in human plasma. NP_{Cis} were incubated in indicated media for 30 min at room temperature, washed, and collected by centrifugation. Corona proteins were resolved on a 12% SDS page. Silica NPs (control) with high corona formation properties served as a positive control.

be small enough to ensure bloodstream circulation while still allowing passive EPR targeting even of poorly permeable tumors and seems optimal for endocytosis-mediated transport.[68−70] To avoid artifacts caused by the fixation procedures of conventional transmission electron microscopy (TEM), we used cryo-EM to confirm shape, size, and homogeneity of our NP_{Cis} (Figure 5c). The neutral ξ-potential of -5.89 ± 6.48 mV accounts for the steric shielding by the pSar layer (Figure 5d). To allow dose matched treatments, cisplatin concentrations were calculated from platinum quantifications, performed by atomic absorption spectroscopy (AAS) using external platinum calibration standards. NP_{Cis} showed a cisplatin concentration of 0.936 g·L^{-1} (3.12 mM), corresponding to a drug loading of 6.8% (w/w) at an overall yield of 47% (Table S4). Successful coupling of cisplatin to pSar$_{160}$-*b*-pGlu(ONa)$_{31}$ was further verified by Fourier-transform infrared spectroscopy (FT-IR) spectroscopy (Figure 5e).

To next investigate that our nanoformulations are capable of also entering low-LRRC8A, cisplatin-resistant cells, we addi-

tionally synthesized Atto647N fluorescently labeled NPs (Ø ~ 50 nm, PDI 0.15) (Figure S12), allowing us to visualize NP trafficking by live cell microscopy (Figure 6). NP uptake in cisplatin sensitive as well as in resistant cells could be confirmed (Figure 6a and Figure S13), and automated quantification by high content microscopy demonstrated its concentration-dependency (Figure S14). These data indicate that resistant cells seem to be more active in endocytosis. Although our RNASeq data indicate differences in metabolic pathways, the mechanistic details need to be investigated in comprehensive follow-up studies. Such aspects might be relevant for drug resistances in general and NP-based targeting of resistant cells. NP uptake was further blocked by the dynamin-dependent endocytosis inhibitor dynasore, confirming NPs' targeting to the endocytic, LRRC8A-independent uptake pathway (Figure 6b). To verify endocytic uptake, which is expected not to be restricted to NP_{Cis}, we also studied fluorescent silica NPs (NP_{Si}, 30 nm). Here, thte endocytic uptake of NP_{Si} was confirmed not only in 2D cell cultures
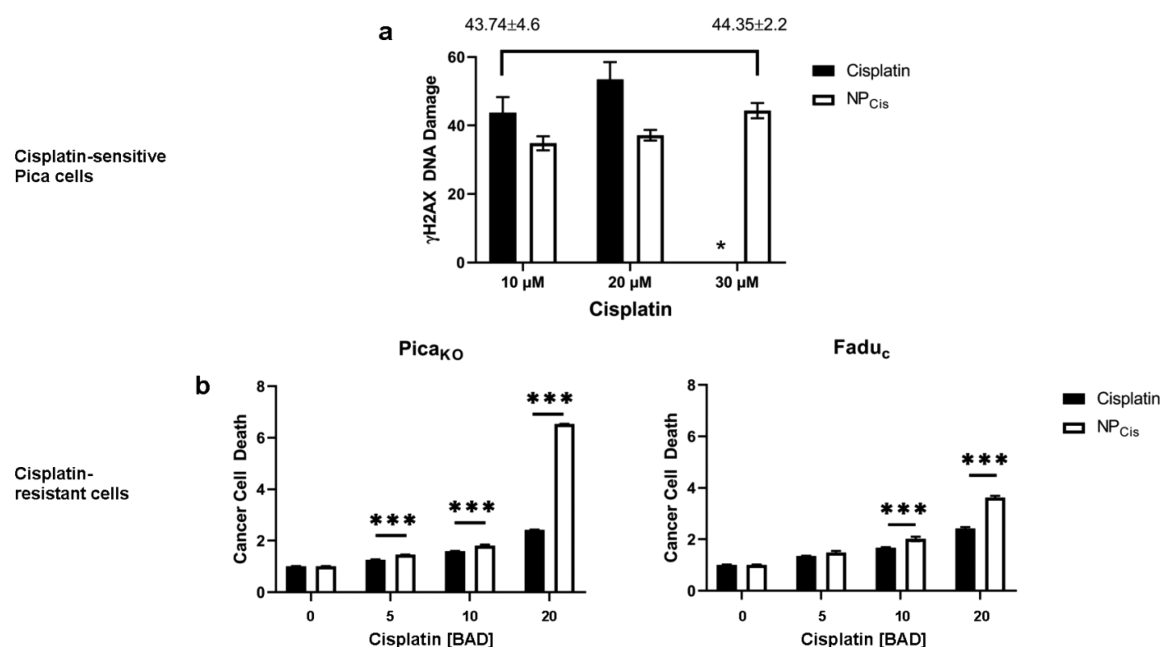
Figure 8. NP$_{Cis}$-treatment can overcome cisplatin resistance. (a) Quantifying cisplatin-induced DNA damage to determine the biologically active dose (BAD) of NP$_{Cis}$ versus free cisplatin in sensitive Pica cells. Cells were treated for 24 h and DNA damage events (γH2AX foci) quantified *via* high-throughput automated microscopy. Similar DNA damage was induced by the standard of care cisplatin (10 μM) or NP$_{Cis}$ (30 μM). *, cells were killed prior to analysis. (b) NP$_{Cis}$ significantly kill cisplatin-resistant HNSCC cells (Pica$_{KO}$/Fadu$_C$). Cells were treated for 48 h, and death was normalized to untreated controls. BAD values (μM; free cisplatin = 1/3 NP$_{Cis}$). Statistical analysis: ***, $p < 0.005$.

(Figure S13) but also importantly in 3D tumor spheroids, mimicking more closely the tumor microarchitecture in patients. Notably, NPs were not only observed in the spheroids' outer cell layers but also deep two-photon microscopy demonstrated that NPs could also penetrate into deeper cell layers (Figure 6c).

NP$_{Cis}$ Show Good Biocompatibility, Enhanced Blood Circulation, Low Toxicity, and Low Corona Formation. Having successfully shown the potential of NP$_{Cis}$ to enter resistant cells independent of the LRRC8A-uptake pathway, we next tested our particles for their general safety profile and biocompatibility (Figure 7). Cells treated with NP$_{Cis}$ or the parent pSar$_{160}$-*b*-pGlu(ONa)$_{31}$ polypept(o)ide did not show any signs of short-term toxicity triggered by the material composition (Figure 7c). In contrast, exposure to silica NPs with high corona formation properties rapidly triggered cell death at higher concentrations (Figure 7c). Moreover, NP$_{Cis}$ did not trigger human macrophage activation, as shown by assessing the induction of IL-1β production (Figure 7a). Again, high corona formation silica NPs strongly induced IL-1β (Figure 7a). Importantly, the exposure of human blood plasma to NP$_{Cis}$ did not lead to activation of the complement system as shown by analyzing complement C5a levels (Figure 7d). In addition, we did not detect aggregation of plasma proteins demonstrated by multiangle DLS analysis (Figure 7e). Consequently, the low toxicity profile paired with no nonspecific activation of macrophages or the complement cascade confirmed the biocompatibility of NP$_{Cis}$, suggesting their potential therapeutic safety also in human settings. These findings are in line with previous reports on the biocompatibility of pSar, whereby complement activation and cytokine induction were not observed.[61,64,71]

To also investigate the NP$_{Cis}$'s potential suitability for intravenous administration, we performed biocompatibility *in vivo* studies employing the ethically less questionable zebrafish embryo model.[62,71−73] *In vivo* imaging microscopy demonstrated that pSar NPs display reduced recognition by the reticuloendothelial system (RES) allowing for prolonged blood circulation (Figure 7b). Here, quantitative fluorescence analysis in zebrafish embryos revealed a circulation half-life of approximately 4 h for fluorescently labeled NP$_{Cis}$ (Figure 7b). The half-life values for NP$_{Cis}$ are lower compared to disulfide cross-linked CCPMs ($\approx$ 12 h) yet comparable to PEGylated liposomes while exceeding non-PEGylated liposomes, as reported previously.[73] Taken together, NP$_{Cis}$ seem suitable for intravenous administration, and the pSar shielding together with the stabilized core architecture provide the basis for passive tumor targeting.

When NPs enter physiological environments, proteins and other biomolecules rapidly bind to the NP surface, leading to the rapid formation of a biomolecule corona. The corona may critically codefine the biological, medical, and pathophysiological identity of NPs, although the mechanistic details have not been resolved in detail.[25−27,30,74] Hence, the design of NPs with low biomolecule adsorption properties seems to be desirable in general, unless a specific 'corona-driven' application is envisaged. Several chemical strategies haven been reported, including our polysarcosine-based approaches with the potential to prevent aggregation, protein corona formation as well as stable blood circulation after intravenous administration.[31,73] Indeed, low corona formation could be verified for NP$_{Cis}$ using human plasma as a relevant model (Figure 7e,f). Collectively, NP$_{Cis}$ are thus based on polypept-(o)ides but resemble NC-6004, which is based on copolymers of PEG-*b*-pGlu(OH) and under clinical evaluation for several malignancies (NC-6004/NCT00910741).[6,42,75,76] Therefore, our approach takes the profit of a clinically relevant cisplatin formulation, translates it to polypeptide(o)ides avoiding the use of PEG, and combines it with aspects of personalized medicine. In addition to the improved therapeutic profile of

pSar,[62−65] from a synthetic perspective, the polypept(o)ide-based design offers the potential to synthesize the polymeric material by sequential monomer addition using living ring-opening N-carboxyanhydride (NCA) polymerization.[60,67,77] This technique may facilitate the industrial scale-up of the block copolymer synthesis. Moreover, NCA polymerization provides easy access to functional end-groups that could be used to introduce targeting moieties, such as antibodies, Fab-fragments, or peptides to enhance or specify the cellular uptake.[21,60,77,78]

Although our findings are most likely of general relevance for other platinum drug nanoformulations, we though wish to emphasize that that we do not claim that our nanoscale cisplatin drug delivery devices are superior to other nano-formulations already in clinical trials, such as NC-6004/NCT00910741. Here, additional (pre)clinical evaluation studies are required.

Application of NP$_{Cis}$ to Break Cisplatin Resistance. Next, we evaluated the potential of our NP$_{Cis}$ to overcome cisplatin resistance. A key issue, which has been neglected in most studies, is the problem of comparing 'free' drug versus NP-based delivered drug concentrations, particularly if these agents enter cells *via* completely different pathways. Here, not only uptake kinetics but also drug-release from NPs and organelles will significantly affect the relevant intracellular biologically active dose (BAD), ultimately triggering effects, such as tumor cell death. Hence, BAD for 1 μM of a free versus 1 μM of a NP-complexed drug will most certainly never be the same.

Consequently, we developed an assay allowing to determine BAD for our agents, by analyzing the levels of DNA damage induced by free cisplatin versus NP$_{Cis}$. As shown in Figure 8a, about 3-fold more NP$_{Cis}$ induced the same levels of DNA damage compared to free cisplatin in wildtype cells (BAD: free cisplatin = 1/3 NP$_{Cis}$). Taking into account the different entry pathways together with the drug-release from NPs and endosomes, such values are expected and relevant for subsequent biological testing, though not reported so far. Thus, we strongly suggest to employ our strategy for studies of other nanoformulated DNA-damaging chemotherapeutics in general.

Importantly, in contrast to free cisplatin as the current standard of care, NP$_{Cis}$ were able to significantly ($p < 0.005$) kill all cisplatin-resistant cells (Figure 8b) by circumventing the LRRC8A-transport pathway and instead exploiting the endocytic delivery route. Again, cytotoxicity correlated well with the induction of DNA-damage, revealed by our objective, automated γH2AX assay (Figure S15). As expected from NP$_{Cis}$'s low corona formation properties (7f), cancer cell killing was similar in the absence or presence of biomolecules. In contrast, the cytotoxicity of silica NPs, showing high protein adsorption, was strongly affected by corona formation (Figures S16 and S17).

Of note, a variety of other (multifunctional) nanoscale platinum drug delivery devices have been developed.[6,17,18] Although we did not test other nanoformulations experimentally, it is expected that they may also be useful to eradicate LRRC8A-based cisplatin-resistant cells, although their cellular uptake and biocompatibility need to be examined. Likewise, multifunctional nanotools, allowing for codeliveries of drugs with siRNAs for specific gene silencing, have been designed in the past, as an approach to increase the power of nano-formulations by targeting proteins, which contribute to

cisplatin resistance due to their overexpression.[11−15] We though demonstrated that low LRRC8A levels are key for cisplatin resistance, and thus, the codelivery of LRRC8A gene silencing siRNA would rather increase instead of breaking resistance and, thus, seems not applicable for our target.

CONCLUSIONS

Despite the current enthusiasm on multifunctional or theranostic nanomedicals, their clinical applicability and superiority compared to drug formulations used in the clinical routine for decades needs to be based on a mechanistic understanding of their advantages. As the field moves away from block-buster treatments of all patients, the need for precision medicine is now accepted and must also to be considered in nanomedicine. We here employed a comprehensive *in silico*, analytical, and *in vitro* experimental pipeline to identify the downregulation of LRRC8A-driven cisplatin uptake as key for cisplatin resistance of HNSCC tumor cells. Likewise, reduced LRRC8A levels seem to be relevant for therapy resistance and the survival of HNSCC cancer patients.[6] To overcome cisplatin resistance, highly biocompatible cisplatin-loaded NPs were constructed, allowing drug delivery *via* the endocytic, LRRC8A-independent, uptake pathway. In direct comparison to cisplatin as the current standard of care, our strategy finally succeeded in killing all cisplatin-resistant cells.

There is ongoing (pre)clinical research to determine if nanoscale platinum drug delivery devices are indeed superior compared to current standard of care formulations in general. Here, an important criteria is the definition and comparison of a biologically active dose (BAD) for nanoparticles versus free drugs that enter cells by different mechanisms, as shown here. Our findings strongly suggest that low-LRRC8A expressing patients should profit most from such platinum nanomedicals. Our findings are most likely of general relevance for other platinum drug nanoformulations. Here, LRRC8A-guided patient stratification is expected to facilitate the evaluation of such clinical trials (such as NC-6004/NCT00910741, driven by the Kataoka group) and, thus, may promote the clinical translation of nanomedicals to overcome chemotherapy resistance (TOC figure).

METHODS/EXPERIMENTAL

Chemicals and Reagents. If not stated otherwise, chemicals were sourced from Sigma-Aldrich/Merck. Cell culture reagents were sourced from Gibco/Thermo Fisher Scientifc. Cell Viability Kits (Cell Titer Glo and Cell Titer Glo 3D) were purchased from Promega. Fluorescent silica NPs were obtained from Kisker Biotech or MSC UG&CoKG. Antibodies were sourced as indicated in Table S1. Clinical cisplatin formulations were sourced from Accord Healthcare GmbH.

Nanoparticle Synthesis and Characterization. The preparation of cisplatin NPs (NP$_{Cis}$) was adapted from the literature and modified by the use of polypept(o)ides of polysacrosine-*block*-poly(L-glutamic acid) (pSar-*b*-pGlu).[67,76,77] For dye-labeled NP$_{Cis}$, cyanine5-amine (1.36 mg, 2.1 μmol, 0.3 equiv) was coupled to pSar-*b*-pGlu (110 mg, 6.9 μmol, 1.0 equiv) *via* 4-(4,6-dimethoxy-1,3,5-triazin-2-yl)-4-methylmorpholinium chloride (DMTMM·Cl) (1.91 mg, 6.9 μmol, 1.0 equiv). All reagents were dissolved in water and stirred at room temperature for 72 h. Purification was performed by dialysis (MWCO 3.5 kDa) with water (+ 1% NaHCO$_3$) and pure water, followed by precipitation in acetone (4500 rpm, 5 min, 4 °C). The product was dried *in vacuo* (91.1 mg, 82%), and the absence of unconjugated dye was verified by HFIP-GPC. The synthesis of pSar-*b*-pGlu was performed as described previously by Steinborn *et al.*[68]

Similarly, block lengths of 160 for pSar and 31 for pGlu were used for NP$_{Cis}$ formation. For the preparation of NP$_{Cis}$, 64.5 mg (4.06 μmol, 1.0 equiv) of pSar160-*b*-pGlu31 was dissolved in Milli-Q water at a concentration of 2.65 g·L^{-1}, corresponding to a pGlu concentration of 5 mmol L^{-1}. After 1 h, a solution of cisplatin (36.5 mg, 121 μmol, 1.0 equiv per Glu) in Milli-Q water was added, and the reaction mixture was placed in a benchtop shaker at 25 °C. After 7 days, the solution was purified from nonconjugated cisplatin by spin-filtration (Amicon Ultra 15, MWCO 100 kDa, 3000 rpm) followed by sterile filtration (Millex GPX 220 nm). The total mass concentration was determined by lyophilization, and pPlatinum quantification was performed by atomic absorption spectroscopy (AAS) using external platinum calibration standards.

To serve as control nanoparticles, core cross-linked polymeric micelles (CCPMs) were prepared from polypept(o)ides of poly-sarcosine-*block*-poly(*S*-ethylsulfonyl-L-cysteine) (pSar-*b*-pCys-(SO$_2$Et)) according to previous reports.[20,21,73] These NPs are covalently labeled with Atto647N and stabilized by disulfide bonds formed from the reactive pCys(SO$_2$Et) block and a lipoic acid-based cross-linker. Here, pSar$_{225}$-*b*-pCys(SO$_2$Et)$_{31}$ was dissolved in dimethyl sulfoxide (DMSO) equipped with 1 M thiourea at a concentration of 7.5 g L^{-1} for 1 h. Next, 20 vol % of 1 mM acetate buffer (pH 4.75) with 10 mM thiourea was added to adjust the concentration to 6.6 g L^{-1}. The solution was left to equilibrate at room temperature for 5 h, followed by dialysis (MWCO 3.5 kDa) against 1 mM acetate buffer (pH 4.75) with 10 mM thiourea. The solution was filtered (GHP 450) and concentrated to 6.6 g L^{-1} by spin filtration (Amicon Ultra, MWCO 3 kDa). For cross-linking, in a separate flask, the liponamide cross-linker was dissolved in ethanol at a concentration of β = 10 g L^{-1} and one equivalent of an aqueous solution of tris(2-carboxyethyl)-phosphine hydrochloride (TCEP·HCl) (50 g L^{-1}) was added. After 18 h, the cross-linker solution was added to the micelle solution at equimolar amounts of thiols per cysteines. After reaction for 48 h at room temperature, unreacted polymer and cross-linker were removed by dialysis against DMSO and Milli-Q water (MWCO 6−8 kDa). For labeling, 0.3 equiv of Atto647 NHS-ester was added per polymer end-group at pH 7.4 (adjusted with 1 M NaHCO$_3$ solution). After 72 h, excess dye was removed by repetitive spin filtration (Amicon Ultra, 100 kDa) using ethanol/water mixtures. The final particle solution (in Milli-Q water) was stored at 4 °C in the dark. The absence of free polymer and free dye was verified by gel permeation chromatography in hexafluoro isopropanol.

Atom Absorption Spectroscopy Measurements. The atom absorption spectroscopy (AAS) measurements were conducted using a PerkinElmer 5100 ZL AA spectrometer with a Zeeman Furnace Module and a Pt hollow cathode lamp at 265.9 nm and air/acetylene mixture.

Dynamic Light Scattering and ζ-Potential Measurements. Single-angle dynamic light scattering (DLS) measurements were performed with a ZetaSizer Nano ZS instrument (Malvern Instruments Ltd., Worcestershire, UK) equipped with a He−Ne laser (λ = 632.8 nm) as the incident beam. All measurements were performed at 25 °C and a detection angle of 173° unless stated otherwise. Disposable polystyrene or PMMA cuvettes (VWR, Darmstadt, Germany) were used for single-angle DLS measurements. Cumulant size, polydispersity index (PDI), and size distribution (intensity weighted) histograms were calculated on the basis of the autocorrelation function of the samples, with automated position and attenuator adjustment at multiple scans. ζ-potential measurements were performed with folded capillary cells (DTS 1061) in aqueous solution containing 3 mM sodium chloride.

Multiangle Dynamic Light Scattering. For multiangle DLS, cylindrical quartz cuvettes (Hellma, Mühlheim, Germany) were cleaned with dust-free distilled acetone and handled in a dust-free flow box. Dynamic light scattering measurements were performed on an ALV spectrometer (ALV-5004, multiple-τ full digital correlator, He−Ne laser (632.8 nm)). To investigate the aggregation behavior of the particles in human plasma, undiluted citrate plasma and the particle solutions were filtered by syringe filters (Millex GS 0.2 μm). The following mixtures were prepared from the particle solutions in

water (β = 5.0 g·L^{-1}): PBS/particle solution 4:1 (β = 1.0 g·L^{-1}), and plasma/particle solution 4:1 (β = 1.0 g·L^{-1}). The cuvettes were incubated for 60 min at 37 °C before measurement at T = 37 °C. The data were analyzed according to the procedure reported by Rausch *et al.*[79] The correlation functions of the plasma measurements were fitted with a triexponential decay function, and the particles were fitted using a sum of two exponentials. The mixtures were fitted by using a sum of both exponential decay functions with or without additional aggregate term.

Infrared Spectroscopy. Attenuated total reflection (ATR) Fourier-transformed infrared (FT-IR) spectroscopy was performed on a Jasco FT-IR 4600 spectrometer with a Jasco ATR Pro ONE unit. Lyophilized solids were measured, and spectra were analyzed by Spectra Manager 2.15.18 (Jasco).

Cryo EM. NP$_{Cis}$ (3.5 μL, 150 mg L^{-1} total solid concentration) were applied to freshly glow discharged quantifoil holey carbon films (R2/1 Cu 200, Quantifoil Micro Tools GmbH), and the grids were blotted for 2.5 s at 100% humidity in a Vitrobot plunge-freezer (FEI Vitrobot Mark III, Thermo Fisher Scientific). Cryo-EM images were recorded on a Talos L120C transmission electron microscope (Thermo Fisher Scientific) operating at 120 kV. The images were recorded at 13 500-, 36 000-, and 73 000-fold magnification.

Cell Culture. Pica cell line was established as described by Mack *et al.*[80] Fadu and THP-1 cell lines were purchased from ATCC (ATCC-HTB43, ATCC-TIB-202). Cell lines were cultured under standard cell culture conditions in their respective media (37 °C, 5% CO$_2$) and subcultured every 3−5 d. Cells were checked for the absence of mycoplasmas using the commercial Venor GeM Advance detection kit (Minerva biolabs) according to manufacturer's instructions. Cells were counted using a Casy Cell Counter and Analyzer TT (Innovatis). For spheroid culture, cells were seeded at a density of 1000 cells per well in round-bottom ultra low-attachment cell culture plates (96-well, Corning) and used 3 d after seeding. THP-1 cells were differentiated into THP-1 M cells at a concentration of 0.5 × 10^6 cells/mL and 50 ng/mL PMA overnight, and then washed with medium twice and used for experiments 48 h postdifferentiation.

Generation of the Conditioned Sub-Cell Lines. For the generation of conditioned subcell line Fadu$_C$, cells were first selected by treatment with high doses of cisplatin corresponding to roughly IC$_{90}$ (5 μM). After the cell line showed constant proliferation under this selection, cells were routinely kept in medium containing cisplatin (3 μM). First experiments were started 6 months after constant conditioning in cisplatin-containing medium.

CRISPR/Cas9 Knockout. PiCa-LRRC8A−/− knockout cells were generated by using the recently described CRISPR/Cas9 tools[81] with the exception that plasmids instead of adenoviruses were used for the delivery of Cas9/sgRNA gene expression cassettes. Plasmids pBbsI-Cas9-OFP-sgLRRC8#1 and pBbsI-Cas9-OFP-sgLRRC8#2 contain the CMV promoter-driven gene expression cassette encoding for *Streptococcus pyogenes* Cas9 nuclease, fused to nuclear-localization sequences, followed by a T2A-linker and orange fluorescent protein OFP. In addition, *LRRC8A*-targeting single-guide RNAs (guide sequences sgRNA-LRRC8A_fw and sgRNA-LRRC8A_rev, see Table S2) are under the control of the human U6 promoter. PiCa cells were transfected with total 2 μg of plasmid DNA and 5 μL of Lipofectamine 2000 reagent using OptiMEM cell culture medium (Gibco) according to manufacturer's instructions (Invitrogen/ThermoFisher). To eliminate nontransfected and nonedited wildtype cells, the transfected cell pool was transferred from 6-well plates to 10 cm dishes 96 h after transfection and 24 h later treated with 2 μg/mL Blasticidin S Hydrochlorid (Fisher Bioreagent) for 9 d. Since the LRRC8 ion channel is responsible for Blasticidin uptake,[82] wildtype cells and nonedited cells (which express functional LRRC8) will not survive Blasticidin treatment, whereas successfully edited *LRRC8A*$^{-/-}$ cells do not express functional LRRC8 ion channels and will therefore survive Blasticidin treatment. From the surviving cell pool, clonal single cell-derived cell lines were generated and successful *LRRC8* gene disruption was confirmed by PCR and subsequent Sanger sequencing. The absence of LRRC8A protein was determined by Western blot analysis.

Single Cell Clone Generation and Characterization. For the generation of single cell-derived cell lines, cells were seeded in round cell culture dishes (Ø 10 cm) at serial dilutions. Dishes were checked for the absence of cell clusters and incubated for 7−10 d. Sterile filter papers were soaked in Trypsin/EDTA before being placed on resulting cell clusters with a minimum distance of about 2 cm. After incubation (5 min, 37 °C), filter papers and any attached cells were transferred to a 24-well cell culture plate with fresh medium and the plate was incubated for another 7−10 days. Samples that showed successful proliferation after this period were used to isolate gDNA (DNeasy Blood & Tissue Kit, Qiagen) and checked by PCR for the correct band lengths. Further analysis was performed after the isolation of RNA (RNeasy Mini Kit, Qiagen) and subsequent transcription to cDNA (Transcriptor First Strand cDNA Synthesis Kit, Roche). All isolation and transcription steps were performed according to manufacturer's instructions. DNA and RNA concentrations were measured on a Nanodrop. PCR analysis was performed on a thermocycler with Taq Polymerase according to manufacturer's instructions. For primer design, see Figure S4.[28,83]

Cell Viability Measurement. Cell viability measurements were performed on a Tecan Spark (Tecan) using the kits CellTiter-Glo 2.0 Viability Assay and CellTiter-Glo 3D Viability Assay according to the manufacturer's instructions. Viability was normalized to control samples incubated under the same conditions. For two-dimensional assays, cells were treated 24 h after seeding in fresh medium containing the respective substances. Viability was assessed 48 h after treatment. For three-dimensional assays, cells were treated 3 d after seeding, after spheroid formation. Half of the culture medium was replaced with fresh medium containing 2× of the target concentration of each substance. After 48 h, another medium change of half the samples volume was performed. The fresh medium contained 1× of the target concentration of each substance. Viability assessment was performed 96 h after initial treatment.

γH2AX-Assay. Cells were counted and seeded in controlled densities (10 000 cells/well) in clear-bottom 96-well plates (Greiner). The immunofluorescence staining of γH2AX was performed after treatment with cisplatin in the given concentrations for 24 h. The cells were then fixed with 4% PFA (20 min, RT) and permeabilized with 0.1% Triton X-100/PBS (10 min, RT). The primary antibody α-γH2AX (rabbit, A300-081A, bethyl) was diluted 2000-fold in 10% FCS/PBS, and the cells stained for 1 h at room temperature. After extensive washing with PBS, Cy3-labeled α-rabbit-antibody was diluted 300-fold in 10% FCS/PBS and incubated with the samples for 1 h at room temperature. The nuclei were stained by the addition of Hoechst 33342 (50 ng/mL) in PBS for 30 min at room temperature after another washing step. The fluorescence signal was quantified on the automated high-content microscopy platform ArrayScan VTI (Thermo Fisher), using the TargetActivation assay at fixed excitation times. The region of interest was defined by the nucleus stain. Each sample was measured in triplicate with at least 5000 cell nuclei analyzed per well. For further information on antibodies and dilutions, see Table S1.

Fluorescence Microscopy. Fluorescence microscopy was performed on a Axiovert 200 M fluorescence microscope (Zeiss) on cells seeded in 35 mm microscopy dishes (MatTek). Depending on further use, cells were either imaged live or fixed with PFA (4%, 20 min room temperature (RT)). Before immunofluorescence staining, cells were permeabilized with Triton X-100 (0.1%, 10 min RT). Antibody staining was performed as described for γH2AX-staining. Hoechst 33342 (50 ng/mL) was used for the staining of nuclei (30 min at RT). For further information on antibodies and dilutions, see Table S1.

Two-Photon Excitation Microscopy. Two-photon excitation (2PE) microscopy was performed to visualize intact spheroids on a Leica TCS SP8 DIVE System (Leica). Image analysis was performed with Leica image suite and ImageJ. To this mean, spheroids were collected 3 d after seeding by gentle centrifugation (100 g, 3 min) and fixed by incubation with 4% PFA at RT (20 min). Cells were then blocked and permeabilized in BSA/PBSTD (PBS, 0.3% Triton X-100, 1% DMSO, 1% BSA). Incubation with the primary antibody, diluted

in 5% FCS/PBSTD (PBS, 0.3% Triton X-100, 1% DMSO), was performed overnight at 4 °C. The secondary antibody, diluted in 5% FCS/PBSTD, was incubated with the sample for 3 h at room temperature. Nuclei were stained by the addition of Hoechst 33342 (50 ng/mL) for 15 min at room temperature. For further information on antibodies and dilutions, see Table S1.

Zebrafish Circulation Studies. The zebrafish embryos were kept in Petri dishes containing zebrafish egg water supplemented with 0.003% phenythiourea (PTU). The Petri dishes were maintained in an incubator at a stable temperature of 28.5 °C. All experiments were performed in accordance with the ethical standards and legislation for animal research in Norway (License FOTS-ID: 13563).

To evaluate the blood circulation of nanoparticles in zebrafish embryos, the protocol described in Dal *et al.* was applied.[73] In short, borosilicate needles for injections were produced using a pipet puller (P-97, Sutter Instrument) and mounted on a micromanipulator (Narishige MN-153) connected to an Eppendorf FemtoJet express pump. Before the injections, the zebrafish embryos were sedated in a tricaine bath (Finquel; 0.02% in zebrafish egg water) and placed on a plate containing hardened agarose gel (2% in water). Two-day old zebrafish embryos were injected in the posterior cardinal vein with 5 nL of the nanoparticle solution. At defined time points (5 min and 1, 4, 24, and 72 h), images were recorded for the whole zebrafish (30× magnification) and the caudal region (120× magnification) using a Leica DFC365FX stereo microscope with a 1.0× plan apo lens. The average fluorescence intensity of the artery region (AF, 30×), normalized by the average total fluorescence of the zebrafish (TF, 120X), was used to determine the nanoparticle circulation in the blood flow. The average artery fluorescence at 5 min (AF-5 min) was considered as 100%, meaning that all nanoparticles were considered to be in circulation at this time point. The obtained values were subtracted by the background fluorescence analyzed in zebrafish injected with PBS.

Antibodies and Western Blot Analysis. For Western Blot analysis, whole cell lysates were prepared in RIPA buffer and samples were separated on a 12% SDS gel. Blotting on to a PVDF membrane was performed with a Trans-Blot Turbo (biorad). After blocking with milk for 1 h at RT, incubation with the primary antibody diluted in milk was performed at 4 °C overnight. Horseradish-peroxidase (HRP)-coupled secondary antibodies were incubated with the blot for 1 h at RT. The detection of luminescence signal after the addition of Clarity Western ECL substrate (biorad) was performed on a ChemiDocTM (biorad). For antibodies and respective dilutions, see Table S1.

Quantification of Complement Component C5a. Complement activation was determined after incubation of 2 μg NP in 20 μL of human plasma (37 °C, 300 rpm, 1 h) with the help of abcam's Human Complement C5a ELISA Kit according to manufacturer's instructions, as has been described in detail.[61]

Clinical Gene Expression and Survival Analysis. Publicly available gene expression data was obtained from The Cancer Genome Atlas (TCGA) Research Network (http://cancergenome.nih.gov/) and assessed *via* the USCS Xena browser.[84] The TCGA Research Network included patients in accordance with the guidelines of the Declaration of Helsinki of 1975, and all patients provided signed informed consent. Data of n = 50 normal adjacent tissue (NAT) and n = 528 HNSCC tissue samples were included. Patients were grouped on the basis of their expression level of LRRC8A, treatment, observation time as indicated, and survival analysis performed as described.[85] Data was visualized with the help of GraphPad PRISM.

Differential Gene Expression Analysis. Cell lysis and RNA isolation was performed using the RNeasy Mini kit (Qiagen, Hilden) according to the manufacturer's instructions. RNA samples (2 μg) were checked for DNA contamination by performing cDNA transcription with and without the addition of reverse transcriptase and then checking for the amplification of housekeeping gene actin in a PCR reaction. For primer sequences, see Table S2. RNA sequencing was performed as described in ref 81. FPKM values to quantify the expression of the RNA sequencing data were calculated using

cufflinks;[86] differential gene expression was performed using deseq2,[87] and the results were visualized by DEBrowser.[88] Further analysis and heatmap plotting of data was performed on graphpad Prism.

ASSOCIATED CONTENT

ⓈⒾ Supporting Information

The Supporting Information is available free of charge at https://pubs.acs.org/doi/10.1021/acsnano.1c08632.

> Discussion of NP corona analysis, figures of flow chart, potential candidates contributing to cisplatin resistance in HNSCC, overall survival of HNSCC patients, verification of LRRC8A-deficient knockout cells, verification of LRRC8A-deficiency, RNA sequencing, overall survival of HNSCC patients, quantification of double-strand breaks, Cy3-signal intensities, LRRC8A-deficient cell lines Pica$_{KO}$ and Fadu$_C$ show no resistance for paclitaxel or doxorubicin and abraxane or caelyx, LRRC8A expression in HNSCC tumors, polysarcosine building blocks forming NP$_{Cis}$ do not show cytotoxicity, CCPM^{Atto647N} design and characterization, uptake of silica nanoparticles, NP$_{Cis}$ induce DNA damage in LRRC8A-deficient cell lines, NP$_{Cis}$ toxicity is independent of corona forming conditions, and silica NP toxicity is dependent on corona forming conditions, and tables of antibodies and dilutions, primer sequences, genetic characterization of LRRC8A knockout clone, quantification of NP$_{Cis}$, RNA sequencing results to identify molecular cisplatin resistance candidates, and candidates relevant for cisplatin resistance identified by RNA sequencing analysis (PDF)

AUTHOR INFORMATION

Corresponding Author

Roland H. Stauber − Nanobiomedicine/ENT Department, University Medical Center Mainz, 55131 Mainz, Germany; ⓞ orcid.org/0000-0002-1341-4523; Email: rstauber@uni-mainz.de

Authors

Svenja Siemer − Nanobiomedicine/ENT Department, University Medical Center Mainz, 55131 Mainz, Germany; ⓞ orcid.org/0000-0003-2089-8949

Tobias A. Bauer − Leiden Academic Center for Drug Research (LACDR), Leiden University, 2333 CC Leiden, The Netherlands; Department of Chemistry, Johannes Gutenberg University, Duesbergweg 10-14, 55099 Mainz, Germany Department of Dermatology, University Medical Center of the Johannes Gutenberg University Mainz, 55131 Mainz, Germany

Paul Scholz − BRAIN AG, 64673 Zwingenberg, Germany

Christina Breder − Nanobiomedicine/ENT Department, University Medical Center Mainz, 55131 Mainz, Germany

Federico Fenaroli − Department of Biosciences, University of Oslo, 0371 Oslo, Norway; ⓞ orcid.org/0000-0002-9060-8786

Gregory Harms − Cell Biology Unit, University Medical Center Mainz, 55131 Mainz, Germany

Dimo Dietrich − Department of Otorhinolaryngology, University Medical Center Bonn, 53127 Bonn, Germany

Jörn Dietrich − Department of Otorhinolaryngology, University Medical Center Bonn, 53127 Bonn, Germany

Christine Rosenauer − Max Planck Institute for Polymer Research, 55128 Mainz, Germany

Matthias Barz − Leiden Academic Center for Drug Research (LACDR), Leiden University, 2333 CC Leiden, The Netherlands; Department of Chemistry, Johannes Gutenberg University, Duesbergweg 10-14, 55099 Mainz, Germany Department of Dermatology, University Medical Center of the Johannes Gutenberg University Mainz, 55131 Mainz, Germany

Sven Becker − Department of Otorhinolaryngology, University Medical Center Tuebingen, 72076 Tuebingen, Germany

Sebastian Strieth − Department of Otorhinolaryngology, University Medical Center Bonn, 53127 Bonn, Germany

Christoph Reinhardt − Center for Thrombosis and Hemostasis (CTH), University Medical Center Mainz, 55131 Mainz, Germany

Torsten Fauth − BRAIN AG, 64673 Zwingenberg, Germany

Jan Hagemann − Nanobiomedicine/ENT Department, University Medical Center Mainz, 55131 Mainz, Germany

Complete contact information is available at:
https://pubs.acs.org/10.1021/acsnano.1c08632

Author Contributions

The manuscript was written through contributions of all authors. All authors have given approval to the final version of the manuscript.

Notes

The authors declare no competing financial interest.

REFERENCES

(1) Wild, C. P.; Weiderpass, E.; Stewart, B. W. *World Cancer Report: Cancer Research for Cancer Prevention*; International Agency for Research on Cancer: Lyon, France, 2020.

(2) Bray, F.; Ferlay, J.; Soerjomataram, I.; Siegel, R. L.; Torre, L. A.; Jemal, A. Global Cancer Statistics 2018: GLOBOCAN Estimates of Incidence and Mortality Worldwide for 36 Cancers in 185 Countries. *Ca-Cancer J. Clin.* **2018**, *68* (6), 394−424.

(3) Niazi, M.; Zakeri-Milani, P.; Najafi Hajivar, S.; Soleymani Goloujeh, M.; Ghobakhlou, N.; Shahbazi Mojarrad, J.; Valizadeh, H. Nano-Based Strategies to Overcome P-Glycoprotein-Mediated Drug Resistance. *Expert Opin. Drug Metab. Toxicol.* **2016**, *12* (9), 1021−33.

(4) Perez-Herrero, E.; Fernandez-Medarde, A. Advanced Targeted Therapies in Cancer: Drug Nanocarriers, the Future of Chemotherapy. *Eur. J. Pharm. Biopharm.* **2015**, *93*, 52−79.

(5) Bar-Zeev, M.; Livney, Y. D.; Assaraf, Y. G. Targeted Nanomedicine for Cancer Therapeutics: Towards Precision Medicine Overcoming Drug Resistance. *Drug Resist. Updates* **2017**, *31*, 15−30.

(6) Uchino, H.; Matsumura, Y.; Negishi, T.; Koizumi, F.; Hayashi, T.; Honda, T.; Nishiyama, N.; Kataoka, K.; Naito, S.; Kakizoe, T. Cisplatin-Incorporating Polymeric Micelles (NC-6004) Can Reduce Nephrotoxicity and Neurotoxicity of Cisplatin in Rats. *Br. J. Cancer* **2005**, *93* (6), 678−87.

(7) Lammers, T.; Kiessling, F.; Hennink, W. E.; Storm, G. Drug Targeting to Tumors: Principles, Pitfalls and (Pre-)Clinical Progress. *J. Controlled Release* **2012**, *161* (2), 175−87.

(8) Dhar, S.; Kolishetti, N.; Lippard, S. J.; Farokhzad, O. C. Targeted Delivery of a Cisplatin Prodrug for Safer and More Effective Prostate Cancer Therapy *in Vivo*. *Proc. Natl. Acad. Sci. U. S. A.* **2011**, *108* (5), 1850−5.

(9) Yang, X. Z.; Du, X. J.; Liu, Y.; Zhu, Y. H.; Liu, Y. Z.; Li, Y. P.; Wang, J. Rational Design of Polyion Complex Nanoparticles to Overcome Cisplatin Resistance in Cancer Therapy. *Adv. Mater.* **2014**, *26* (6), 931−6.

(10) Mi, P.; Miyata, K.; Kataoka, K.; Cabral, H. Clinical Translation of Self-Assembled Cancer Nanomedicines. *Adv. Ther-Germany* **2021**, *4* (1), 2000159.

(11) Lin, Y. X.; Wang, Y.; An, H. W.; Qi, B.; Wang, J.; Wang, L.; Shi, J.; Mei, L.; Wang, H. Peptide-Based Autophagic Gene and Cisplatin Co-Delivery Systems Enable Improved Chemotherapy Resistance. *Nano Lett.* **2019**, *19* (5), 2968−2978.

(12) Xu, X.; Xie, K.; Zhang, X. Q.; Pridgen, E. M.; Park, G. Y.; Cui, D. S.; Shi, J.; Wu, J.; Kantoff, P. W.; Lippard, S. J.; Langer, R.; Walker, G. C.; Farokhzad, O. C. Enhancing Tumor Cell Response to Chemotherapy through Nanoparticle-Mediated Codelivery of siRNA and Cisplatin Prodrug. *Proc. Natl. Acad. Sci. U. S. A.* **2013**, *110* (46), 18638−43.

(13) Dhar, S.; Gu, F. X.; Langer, R.; Farokhzad, O. C.; Lippard, S. J. Targeted Delivery of Cisplatin to Prostate Cancer Cells by Aptamer Functionalized Pt(IV) Prodrug-PLGA-PEG Nanoparticles. *Proc. Natl. Acad. Sci. U. S. A.* **2008**, *105* (45), 17356−61.

(14) Blanco, M. D.; Teijon, C.; Olmo, R. M.; Teijon, J. M. Targeted Nanoparticles for Cancer Therapy. In *Recent Advantages in Novel Drug Carrier Systems*; Sezer, A. D., Ed.; BoD - Books on Demand: Rijeka, Croatia, 2012; pp 241−280.

(15) Martinez, A.; Muniz, E.; Teijon, C.; Iglesias, I.; Teijon, J. M.; Blanco, M. D. Targeting Tamoxifen to Breast Cancer Xenograft Tumours: Preclinical Efficacy of Folate-Attached Nanoparticles Based on Alginate-Cysteine/Disulphide-Bond-Reduced Albumin. *Pharm. Res.* **2014**, *31* (5), 1264−1274.

(16) Li, Y.; Deng, Y.; Tian, X.; Ke, H.; Guo, M.; Zhu, A.; Yang, T.; Guo, Z.; Ge, Z.; Yang, X.; Chen, H. Multipronged Design of Light-Triggered Nanoparticles to Overcome Cisplatin Resistance for Efficient Ablation of Resistant Tumor. *ACS Nano* **2015**, *9* (10), 9626−37.

(17) Johnstone, T. C.; Suntharalingam, K.; Lippard, S. J. The Next Generation of Platinum Drugs: Targeted Pt(II) Agents, Nanoparticle Delivery, and Pt(IV) Prodrugs. *Chem. Rev.* **2016**, *116* (5), 3436−86.

(18) van der Meel, R.; Sulheim, E.; Shi, Y.; Kiessling, F.; Mulder, W. J. M.; Lammers, T. Smart Cancer Nanomedicine. *Nat. Nanotechnol.* **2019**, *14* (11), 1007−1017.

(19) Mochida, Y.; Cabral, H.; Kataoka, K. Polymeric Micelles for Targeted Tumor Therapy of Platinum Anticancer Drugs. *Expert Opin. Drug Delivery* **2017**, *14* (12), 1423−1438.

(20) Klinker, K.; Schafer, O.; Huesmann, D.; Bauer, T.; Capeloa, L.; Braun, L.; Stergiou, N.; Schinnerer, M.; Dirisala, A.; Miyata, K.; Osada, K.; Cabral, H.; Kataoka, K.; Barz, M. Secondary-Structure-Driven Self-Assembly of Reactive Polypept(o)ides: Controlling Size, Shape, and Function of Core Cross-Linked Nanostructures. *Angew. Chem., Int. Ed.* **2017**, *56* (32), 9608−9613.

(21) Schafer, O.; Klinker, K.; Braun, L.; Huesmann, D.; Schultze, J.; Koynov, K.; Barz, M. Combining Orthogonal Reactive Groups in Block Copolymers for Functional Nanoparticle Synthesis in a Single Step. *ACS Macro Lett.* **2017**, *6* (10), 1140−1145.

(22) Nishiyama, N.; Kato, Y.; Sugiyama, Y.; Kataoka, K. Cisplatin-Loaded Polymer-Metal Complex Micelle with Time-Modulated Decaying Property as a Novel Drug Delivery System. *Pharm. Res.* **2001**, *18* (7), 1035−41.

(23) Atrafi, F.; van Eerden, R. A. G.; Koolen, S. L. W.; de Bruijn, P.; Rijcken, C. J. F.; Hanssen, R.; Eskens, F.; Lolkema, M. P.; Oomen-de Hoop, E.; Damman, J.; Mathijssen, R. H. J. Docetaxel Skin Exposure and Micronucleation Contributes to Skin Toxicity Caused by CPC634. *Cancers* **2021**, *13* (15), 3741.

(24) Stauber, R. H.; Westmeier, D.; Wandrey, M.; Becker, S.; Docter, D.; Ding, G. B.; Thines, E.; Knauer, S. K.; Siemer, S. Mechanisms of Nanotoxicity - Biomolecule Coronas Protect Pathological Fungi against Nanoparticle-Based Eradication. *Nanotoxicology* **2020**, *14* (9), 1157.

(25) Gianneli, M.; Polo, E.; Lopez, H.; Castagnola, V.; Aastrup, T.; Dawson, K. A. Label-Free In-Flow Detection of Receptor Recognition Motifs on the Biomolecular Corona of Nanoparticles. *Nanoscale* **2018**, *10* (12), 5474−5481.

(26) Walkey, C. D.; Olsen, J. B.; Song, F.; Liu, R.; Guo, H.; Olsen, D. W.; Cohen, Y.; Emili, A.; Chan, W. C. Protein Corona Fingerprinting Predicts the Cellular Interaction of Gold and Silver Nanoparticles. *ACS Nano* **2014**, *8* (3), 2439−55.

(27) Hadjidemetriou, M.; Al-Ahmady, Z.; Kostarelos, K. Time-Evolution of *in Vivo* Protein Corona onto Blood-Circulating PEGylated Liposomal Doxorubicin (DOXIL) Nanoparticles. *Nanoscale* **2016**, *8* (13), 6948−57.

(28) Westmeier, D.; Posselt, G.; Hahlbrock, A.; Bartfeld, S.; Vallet, C.; Abfalter, C.; Docter, D.; Knauer, S. K.; Wessler, S.; Stauber, R. H. Nanoparticle Binding Attenuates the Pathobiology of Gastric Cancer-Associated *Helicobacter pylori*. *Nanoscale* **2018**, *10* (3), 1453−1463.

(29) Docter, D.; Strieth, S.; Westmeier, D.; Hayden, O.; Gao, M.; Knauer, S. K.; Stauber, R. H. No King without a Crown–Impact of the Nanomaterial-Protein Corona on Nanobiomedicine. *Nanomedicine (London, U. K.)* **2015**, *10* (3), 503−19.

(30) Kreyling, W. G.; Abdelmonem, A. M.; Ali, Z.; Alves, F.; Geiser, M.; Haberl, N.; Hartmann, R.; Hirn, S.; de Aberasturi, D. J.; Kantner, K.; Khadem-Saba, G.; Montenegro, J. M.; Rejman, J.; Rojo, T.; de Larramendi, I. R.; Ufartes, R.; Wenk, A.; Parak, W. J. *In Vivo* Integrity of Polymer-Coated Gold Nanoparticles. *Nat. Nanotechnol.* **2015**, *10* (7), 619−23.

(31) Alberg, I.; Kramer, S.; Schinnerer, M.; Hu, Q.; Seidl, C.; Leps, C.; Drude, N.; Mockel, D.; Rijcken, C.; Lammers, T.; Diken, M.; Maskos, M.; Morsbach, S.; Landfester, K.; Tenzer, S.; Barz, M.; Zentel, R. Polymeric Nanoparticles with Neglectable Protein Corona. *Small* **2020**, *16* (18), 1907574.

(32) Alberg, I.; Kramer, S.; Leps, C.; Tenzer, S.; Zentel, R. Effect of Core-Crosslinking on Protein Corona Formation on Polymeric Micelles. *Macromol. Biosci.* **2021**, *21* (4), 2000414.

(33) Vinogradov, S.; Wei, X. Cancer Stem Cells and Drug Resistance: The Potential of Nanomedicine. *Nanomedicine (London, U. K.)* **2012**, *7* (4), 597−615.

(34) Alsahafi, E.; Begg, K.; Amelio, I.; Raulf, N.; Lucarelli, P.; Sauter, T.; Tavassoli, M. Clinical Update on Head and Neck Cancer: Molecular Biology and Ongoing Challenges. *Cell Death Dis.* **2019**, *10* (8), 540.

(35) Price, K. A.; Cohen, E. E. Current Treatment Options for Metastatic Head and Neck Cancer. *Curr. Treat Options Oncol* **2012**, *13* (1), 35−46.

(36) Oosting, S. F.; Haddad, R. I. Best Practice in Systemic Therapy for Head and Neck Squamous Cell Carcinoma. *Front. Oncol.* **2019**, *9*, 815.

(37) Galluzzi, L.; Senovilla, L.; Vitale, I.; Michels, J.; Martins, I.; Kepp, O.; Castedo, M.; Kroemer, G. Molecular Mechanisms of Cisplatin Resistance. *Oncogene* **2012**, *31* (15), 1869−83.

(38) Bagrodia, A.; Lee, B. H.; Lee, W.; Cha, E. K.; Sfakianos, J. P.; Iyer, G.; Pietzak, E. J.; Gao, S. P.; Zabor, E. C.; Ostrovnaya, I.; Kaffenberger, S. D.; Syed, A.; Arcila, M. E.; Chaganti, R. S.; Kundra, R.; Eng, J.; Hreiki, J.; Vacic, V.; Arora, K.; Oschwald, D. M.; et al. Genetic Determinants of Cisplatin Resistance in Patients with Advanced Germ Cell Tumors. *J. Clin. Oncol.* **2016**, *34* (33), 4000−4007.

(39) Zhu, S.; Shanbhag, V.; Wang, Y.; Lee, J.; Petris, M. A Role for the ATP7A Copper Transporter in Tumorigenesis and Cisplatin Resistance. *J. Cancer* **2017**, *8* (11), 1952−1958.

(40) Siddik, Z. H. Cisplatin: Mode of Cytotoxic Action and Molecular Basis of Resistance. *Oncogene* **2003**, *22* (47), 7265−79.

(41) Holohan, C.; Van Schaeybroeck, S.; Longley, D. B.; Johnston, P. G. Cancer Drug Resistance: An Evolving Paradigm. *Nat. Rev. Cancer* **2013**, *13* (10), 714−26.

(42) Rottenberg, S.; Disler, C.; Perego, P. The Rediscovery of Platinum-Based Cancer Therapy. *Nat. Rev. Cancer* **2021**, *21* (1), 37−50.

(43) Jou, A.; Hess, J. Epidemiology and Molecular Biology of Head and Neck Cancer. *Oncol. Res. Treat.* **2017**, *40* (6), 328−332.

(44) Sacco, A. G.; Cohen, E. E. Current Treatment Options for Recurrent or Metastatic Head and Neck Squamous Cell Carcinoma. *J. Clin. Oncol.* **2015**, *33* (29), 3305−13.

(45) Lammers, T.; Kiessling, F.; Ashford, M.; Hennink, W.; Crommelin, D.; Storm, G. Cancer Nanomedicine: Is Targeting Our Target? *Nat. Rev. Mater.* **2016**, *1* (9), 16069.

(46) Cameron, D.; Piccart-Gebhart, M. J; Gelber, R. D; Procter, M.; Goldhirsch, A.; de Azambuja, E.; Castro, G.; Untch, M.; Smith, I.; Gianni, L.; Baselga, J.; Al-Sakaff, N.; Lauer, S.; McFadden, E.; Leyland-Jones, B.; Bell, R.; Dowsett, M.; Jackisch, C. 11 Years' Follow-Up of Trastuzumab after Adjuvant Chemotherapy in HER2-Positive Early Breast Cancer: Final Analysis of the HERceptin Adjuvant (HERA) Trial. *Lancet* **2017**, *389* (10075), 1195−1205.

(47) Swain, S. M.; Baselga, J.; Kim, S.-B.; Ro, J.; Semiglazov, V.; Campone, M.; Ciruelos, E.; Ferrero, J.-M.; Schneeweiss, A.; Heeson, S.; Clark, E.; Ross, G.; Benyunes, M. C.; Cortes, J. Pertuzumab, Trastuzumab, and Docetaxel in HER2-Positive Metastatic Breast Cancer. *N. Engl. J. Med.* **2015**, *372* (8), 724−734.

(48) Humblet, Y. Cetuximab: An IgG(1) Monoclonal Antibody for the Treatment of Epidermal Growth Factor Receptor-Expressing Tumours. *Expert Opin. Pharmacother.* **2004**, *5* (7), 1621−33.

(49) Ferrer, I.; Zugazagoitia, J.; Herbertz, S.; John, W.; Paz-Ares, L.; Schmid-Bindert, G. KRAS-Mutant Non-Small Cell Lung Cancer: From Biology to Therapy. *Lung Cancer* **2018**, *124*, 53−64.

(50) Kelland, L. The Resurgence of Platinum-Based Cancer Chemotherapy. *Nat. Rev. Cancer* **2007**, *7* (8), 573−84.

(51) Heijink, A. M.; Everts, M.; Honeywell, M. E.; Richards, R.; Kok, Y. P.; de Vries, E. G. E.; Lee, M. J.; van Vugt, M. Modeling of Cisplatin-Induced Signaling Dynamics in Triple-Negative Breast Cancer Cells Reveals Mediators of Sensitivity. *Cell Rep.* **2019**, *28* (9), 2345−2357.

(52) Wu, G.; Haw, R. Functional Interaction Network Construction and Analysis for Disease Discovery. *Methods Mol. Biol.* **2017**, *1558*, 235−253.

(53) Sorensen, B. H.; Dam, C. S.; Sturup, S.; Lambert, I. H. Dual Role of LRRC8A-Containing Transporters on Cisplatin Resistance in Human Ovarian Cancer Cells. *J. Inorg. Biochem.* **2016**, *160*, 287−95.

(54) Sonego, M.; Pellizzari, I.; Dall'Acqua, A.; Pivetta, E.; Lorenzon, I.; Benevol, S.; Bomben, R.; Spessotto, P.; Sorio, R.; Gattei, V.; Belletti, B.; Schiappacassi, M.; Baldassarre, G. Common Biological Phenotypes Characterize the Acquisition of Platinum-Resistance in Epithelial Ovarian Cancer Cells. *Sci. Rep.* **2017**, *7* (1), 7104.

(55) Sorensen, B. H.; Nielsen, D.; Thorsteinsdottir, U. A.; Hoffmann, E. K.; Lambert, I. H. Downregulation of LRRC8A Protects Human Ovarian and Alveolar Carcinoma Cells against Cisplatin-Induced Expression of p53, MDM2, p21Waf1/Cip1, and Caspase-9/-3 Activation. *Am. J. Physiol Cell Physiol* **2016**, *310* (11), C857−73.

(56) Voss, F. K.; Ullrich, F.; Munch, J.; Lazarow, K.; Lutter, D.; Mah, N.; Andrade-Navarro, M. A.; von Kries, J. P.; Stauber, T.; Jentsch, T. J. Identification of LRRC8 Heteromers as an Essential Component of the Volume-Regulated Anion Channel VRAC. *Science* **2014**, *344* (6184), 634−8.

(57) Jentsch, T. J.; Lutter, D.; Planells-Cases, R.; Ullrich, F.; Voss, F. K. VRAC: Molecular Identification as LRRC8 Heteromers with Differential Functions. *Pfluegers Arch.* **2016**, *468* (3), 385−93.

(58) Planells-Cases, R.; Lutter, D.; Guyader, C.; Gerhards, N. M.; Ullrich, F.; Elger, D. A.; Kucukosmanoglu, A.; Xu, G.; Voss, F. K.; Reincke, S. M.; Stauber, T.; Blomen, V. A.; Vis, D. J.; Wessels, L. F.; Brummelkamp, T. R.; Borst, P.; Rottenberg, S.; Jentsch, T. J. Subunit Composition of VRAC Channels Determines Substrate Specificity and Cellular Resistance to Pt-Cased Anti-Cancer Drugs. *EMBO J.* **2015**, *34* (24), 2993−3008.

(59) Bao, J.; Perez, C. J.; Kim, J.; Zhang, H.; Murphy, C. J.; Hamidi, T.; Jaubert, J.; Platt, C. D.; Chou, J.; Deng, M.; Zhou, M. H.; Huang, Y.; Gaitan-Penas, H.; Guenet, J. L.; Lin, K.; Lu, Y.; Chen, T.; Bedford, M. T.; Dent, S. Y.; Richburg, J. H. Deficient LRRC8A-Dependent Volume-Regulated Anion Channel Activity Is Associated with Male Infertility in Mice. *JCI Insight* **2018**, *3* (16), No. e99767.

(60) Birke, A.; Ling, J.; Barz, M. Polysarcosine-Containing Copolymers: Synthesis, Characterization, Self-Assembly, and Applications. *Prog. Polym. Sci.* **2018**, *81*, 163−208.

(61) Weber, B.; Birke, A.; Fischer, K.; Schmidt, M.; Barz, M. Solution Properties of Polysarcosine: From Absolute and Relative Molar Mass Determinations to Complement Activation. *Macromolecules* **2018**, *51* (7), 2653−2661.

(62) Son, K.; Ueda, M.; Taguchi, K.; Maruyama, T.; Takeoka, S.; Ito, Y. Evasion of the Accelerated Blood Clearance Phenomenon by Polysarcosine Coating of Liposomes. *J. Controlled Release* **2020**, *322*, 209−216.

(63) Shiraishi, K.; Kawano, K.; Maitani, Y.; Aoshi, T.; Ishii, K. J.; Sanada, Y.; Mochizuki, S.; Sakurai, K.; Yokoyama, M. Exploring the Relationship between Anti-PEG IgM Behaviors and PEGylated Nanoparticles and Its Significance for Accelerated Blood Clearance. *J. Controlled Release* **2016**, *234*, 59−67.

(64) Nogueira, S. S.; Schlegel, A.; Maxeiner, K.; Weber, B.; Barz, M.; Schroer, M. A.; Blanchet, C. E.; Svergun, D. I.; Ramishetti, S.; Peer, D.; Langguth, P.; Sahin, U.; Haas, H. Polysarcosine-Functionalized Lipid Nanoparticles for Therapeutic mRNA Delivery. *Acs Appl. Nano Mater.* **2020**, *3* (11), 10634−10645.

(65) Barz, M.; Luxenhofer, R.; Zentel, R.; Vicent, M. J. Overcoming the PEG-Addiction: Well-Defined Alternatives to PEG, from Structure-Property Relationships to Better Defined Therapeutics. *Polym. Chem.* **2011**, *2* (9), 1900−1918.

(66) Li, A.; Zhang, D. Synthesis and Characterization of Cleavable Core-Cross-Linked Micelles Based on Amphiphilic Block Copolypeptoids as Smart Drug Carriers. *Biomacromolecules* **2016**, *17* (3), 852−61.

(67) Birke, A.; Huesmann, D.; Kelsch, A.; Weilbacher, M.; Xie, J.; Bros, M.; Bopp, T.; Becker, C.; Landfester, K.; Barz, M. Polypeptoid-Block-Polypeptide Copolymers: Synthesis, Characterization, and Application of Amphiphilic Block Copolypept(o)ides in Drug Formulations and Miniemulsion Techniques. *Biomacromolecules* **2014**, *15* (2), 548−57.

(68) Steinborn, B.; Hirschle, P.; Hohn, M.; Bauer, T.; Barz, M.; Wuttke, S.; Wagner, E.; Lachelt, U. Core-Shell Functionalized Zirconium-Pemetrexed Coordination Nanoparticles as Carriers with a High Drug Content. *Adv. Ther-Germany* **2019**, *2* (11), 1900120.

(69) Cabral, H.; Matsumoto, Y.; Mizuno, K.; Chen, Q.; Murakami, M.; Kimura, M.; Terada, Y.; Kano, M. R.; Miyazono, K.; Uesaka, M.; Nishiyama, N.; Kataoka, K. Accumulation of Sub-100 nm Polymeric Micelles in Poorly Permeable Tumours Depends on Size. *Nat. Nanotechnol.* **2011**, *6* (12), 815−23.

(70) Ye, H.; Shen, Z.; Yu, L.; Wei, M.; Li, Y. Manipulating Nanoparticle Transport within Blood Flow through External Forces: An Exemplar of Mechanics in Nanomedicine. *Proc. R. Soc. London, Ser. A* **2018**, *474* (2211), 20170845.

(71) Bleher, S.; Buck, J.; Muhl, C.; Sieber, S.; Barnert, S.; Witzigmann, D.; Huwyler, J.; Barz, M.; Suss, R. Poly(sarcosine) Surface Modification Imparts Stealth-Like Properties to Liposomes. *Small* **2019**, *15* (50), 1904716.

(72) Kurihara, K.; Ueda, M.; Hara, I.; Ozeki, E.; Togashi, K.; Kimura, S. Control of *in Vivo* Disposition and Immunogenicity of Polymeric Micelles by Adjusting Poly(sarcosine) Chain Lenghts on Surface. *J. Nanopart. Res.* **2017**, *19* (7), 242.

(73) Dal, N. J. K.; Kocere, A.; Wohlmann, J.; Van Herck, S.; Bauer, T. A.; Resseguier, J.; Bagherifam, S.; Hyldmo, H.; Barz, M.; De Geest, B. G.; Fenaroli, F. Zebrafish Embryos Allow Prediction of Nanoparticle Circulation Times in Mice and Facilitate Quantification of Nanoparticle-Cell Interactions. *Small* **2020**, *16* (5), 1906719.

(74) Tenzer, S.; Docter, D.; Kuharev, J.; Musyanovych, A.; Fetz, V.; Hecht, R.; Schlenk, F.; Fischer, D.; Kiouptsi, K.; Reinhardt, C.; Landfester, K.; Schild, H.; Maskos, M.; Knauer, S. K.; Stauber, R. H. Rapid Formation of Plasma Protein Corona Critically Affects Nanoparticle Pathophysiology. *Nat. Nanotechnol.* **2013**, *8* (10), 772−81.

(75) Mochida, Y.; Cabral, H.; Miura, Y.; Albertini, F.; Fukushima, S.; Osada, K.; Nishiyama, N.; Kataoka, K. Bundled Assembly of Helical Nanostructures in Polymeric Micelles Loaded with Platinum Drugs Enhancing Therapeutic Efficiency against Pancreatic Tumor. *ACS Nano* **2014**, *8* (7), 6724−38.

(76) Nishiyama, N.; Okazaki, S.; Cabral, H.; Miyamoto, M.; Kato, Y.; Sugiyama, Y.; Nishio, K.; Matsumura, Y.; Kataoka, K. Novel Cisplatin-Incorporated Polymeric Micelles Can Eradicate Solid Tumors in Mice. *Cancer Res.* **2003**, *63* (24), 8977−8983.

(77) Klinker, K.; Barz, M. Polypept(o)ides: Hybrid Systems Based on Polypeptides and Polypeptoids. *Macromol. Rapid Commun.* **2015**, *36* (22), 1943−57.

(78) Kappel, C.; Seidl, C.; Medina-Montano, C.; Schinnerer, M.; Alberg, I.; Leps, C.; Sohl, J.; Hartmann, A. K.; Fichter, M.; Kuske, M.; Schunke, J.; Kuhn, G.; Tubbe, I.; Passlick, D.; Hobernik, D.; Bent, R.; Haas, K.; Montermann, E.; Walzer, K.; Diken, M.; et al. Density of Conjugated Antibody Determines the Extent of Fc Receptor Dependent Capture of Nanoparticles by Liver Sinusoidal Endothelial Cells. *ACS Nano* **2021**, *15* (9), 15191.

(79) Rausch, K.; Reuter, A.; Fischer, K.; Schmidt, M. Evaluation of Nanoparticle Aggregation in Human Blood Serum. *Biomacromolecules* **2010**, *11* (11), 2836−9.

(80) Mack, B.; Eggert, C.; Eder, K.; Imrich, S.; Baumeister, P.; Harreus, U.; Gires, O. Rapid and Non-Enzymatic *in Vitro* retrieval of Tumour Cells from Surgical Specimens. *PLoS One* **2013**, *8* (1), e55540.

(81) Trothe, J.; Ritzmann, D.; Lang, V.; Scholz, P.; Pul, U.; Kaufmann, R.; Buerger, C.; Ertongur-Fauth, T. Hypotonic Stress Response of Human Keratinocytes Involves LRRC8A as Component of Volume-Regulated Anion Channels. *Exp. Dermatol.* **2018**, *27* (12), 1352−1360.

(82) Lee, C. C.; Freinkman, E.; Sabatini, D. M.; Ploegh, H. L. The Protein Synthesis Inhibitor Blasticidin S Enters Mammalian Cells *via* Leucine-Rich Repeat-Containing Protein 8D. *J. Biol. Chem.* **2014**, *289* (24), 17124−31.

(83) Stauber, R. H.; Knauer, S. K.; Habtemichael, N.; Bier, C.; Unruhe, B.; Weisheit, S.; Spange, S.; Nonnenmacher, F.; Fetz, V.; Ginter, T.; Reichardt, S.; Liebmann, C.; Schneider, G.; Kramer, O. H. A Combination of a Ribonucleotide Reductase Inhibitor and Histone Deacetylase Inhibitors Downregulates EGFR and Triggers BIM-Dependent Apoptosis in Head and Neck Cancer. *Oncotarget* **2012**, *3* (1), 31−43.

(84) Goldman, M. J.; Craft, B.; Hastie, M.; Repecka, K.; McDade, F.; Kamath, A.; Banerjee, A.; Luo, Y.; Rogers, D.; Brooks, A. N.; Zhu, J.; Haussler, D. Visualizing and Interpreting Cancer Genomics Data *via* the Xena Platform. *Nat. Biotechnol.* **2020**, *38* (6), 675−678.

(85) Bockhorst, C.; Dietrich, J.; Vogt, T. J.; Stauber, R. H.; Strieth, S.; Bootz, F.; Dietrich, D.; Vos, L. The DNA Methylation Landscape of PD-1 (PDCD1) and Adjacent lncRNA AC131097.3 in Head and Neck Squamous Cell Carcinoma. *Epigenomics* **2021**, *13* (2), 113−127.

(86) Trapnell, C.; Roberts, A.; Goff, L.; Pertea, G.; Kim, D.; Kelley, D. R.; Pimentel, H.; Salzberg, S. L.; Rinn, J. L.; Pachter, L. Differential Gene and Transcript Expression Analysis of RNA-Seq Experiments with TopHat and Cufflinks. *Nat. Protoc.* **2012**, *7* (3), 562−78.

(87) Love, M. I.; Huber, W.; Anders, S. Moderated Estimation of Fold Change and Dispersion for RNA-Seq Data with DESeq2. *Genome Biol.* **2014**, *15* (12), 550.

(88) Kucukural, A.; Yukselen, O.; Ozata, D. M.; Moore, M. J.; Garber, M. DEBrowser: Interactive Differential Expression Analysis and Visualization Tool for Count Data. *BMC Genomics* **2019**, *20* (1), 6.